

Politecnico di Torino

Corso di Laurea Magistrale in

Mechanical Engineering

Development of correlations for the heat losses from the receivers of modular CSP plants with central tower



**Politecnico
di Torino**

supervisor: prof. Laura Savoldi

candidate: Dong Xuezhong

Academic year 2020/2021

ABSTRACT

The analysis in this work is based on a sodium cooled, billboard type receiver adopted in CSP plant for Jemalong (Australia) Solar Thermal Station. It is aimed to evaluate the convective heat losses for the irrational surface of the receiver by using 3D computational fluid dynamics (CFD).

The computational results for free convection are first being analyzed when imposing different uniform surface temperature for the receiver and a correlation procedure based on dimensionless Nusselt number on dependency of Rayleigh number is conducted. Then simulations for pure forced convection under different wind direction and intensity are being set up with gravity off and directional wind effect on heat losses has been analyzed. The correlation procedure for evaluating convective heat losses is done after determination of characteristic length by observing temperature and velocity fields around the receiver. A discover of similar dynamics behavior regarding supplementary incidence angle has been revealed.

At the end, a mixed convection analysis is made to verify the accuracy of obtained correlations by comparing the results of heat transfer coefficient between that calculated from correlation and that from simulations.

Keywords: central tower system, CSP, billboard type receiver, sodium, CFD, convective heat losses

Table of contents

NOMENCLATURE	0
CHAPTER ONE INTRODUCTION	2
1.1 CSP and central tower receivers	2
1.2 The issue of efficiency	3
1.3 The Jemalong receiver and previous attempts to evaluate losses	4
1.4 Aim of the work	6
CHAPTER TWO COMPUTATIONAL MODEL	7
2.1 Computational domain	7
2.2 CFD grid	8
2.3 Turbulence closure	10
2.4 Simulation setup	10
CHAPTER THREE ANALYSIS OF FREE CONVECTION LOSSES	11
3.1 Convective heat transfer correlation	11
3.2 Characteristic lengths for the heat transfer	13
3.3 Main features of the computed results	14
3.4 From HTC to Nu correlation	17
CHAPTER FOUR ANALYSIS OF LOSSES DUE TO WIND	20
4.1 Analysis of forced convection when facing frontal wind	20
4.1.1 Boundary conditions and simulation setup	20
4.1.2 Main features of computed results	22
4.1.3 Evaluation of characteristic length	24
4.1.4 From HTC to Nu correlation	26
4.2 Analysis for forced convection when wind is coming from other directions -wind direction effect	28

4.2.1 Velocity fields of computed results	29
4.2.2 Evaluation of characteristic length	31
4.2.3 Similarity of characteristic length correlated to incidence angle	37
4.2.4 From HTC to Nu correlations	38
CHAPTER FIVE ANALYSIS OF LOSSES IN MIXED FLOW REGIME	44
5.1 Mixed convection estimation	44
5.2 Simulation setting and the main features of the computed results.....	45
CHAPTER SIX CONCLUSIONS	49
ACKNOWLEDGEMENTS	51
REFERENCES	52

List of figures

Figure 1.1 Jemalong solar thermal station: overview.	4
Figure 1.2 Jemalong solar thermal station: solar receiver on one tower.....	4
Figure 1.3 Jemalong solar receiver: simplified CAD model.....	5
Figure 2.1 Computational CFD domain adopted in the present study.....	7
Figure 2.2 Example of the computational CFD domain adopted for the simulations with wind direction of 30°.	8
Figure 2.3 Mesh domain, vertical section	9
Figure 2.4 Mesh domain, horizontal section.....	9
Figure 3.1 Procedure adopted in this work to compute the Nusselt number from CFD results.....	12
Figure 3.2 Main dimensions for expressing the characteristic length. W is defined as the width of the surface that will be used in wind direction problem., H as the height of the surface that will be used in free convection analysis and in wind effect analysis.	13
Figure 3.3 Temperature fields for natural convection when T=907K. vertical (a) and horizontal (b) section views.....	15
Figure 3.4 Vertical temperature fields zoomed near the edge of the hot surface.....	16
Figure 3.5 Vertical section velocity vector field for natural convection when T=907K.....	16
Figure 3.6 Velocity vector field from the section parallel to the hot surface.....	17
Figure 3.7 Ln (Nu) as function of Ln (Ra) plot for the free convection computed results	19
Figure 4.1 Computational domain and boundary conditions when wind comes from frontal direction	21
Figure 4.2 Pressure field computed on a vertical section when T=907K and v=5m/s	22
Figure 4.3 Velocity field computed when T=907K, v=5m/s, frontal wind, lateral view.....	22
Figure 4.4 Corner stagnation phenomena, zoomed pressure field (a) and zoomed velocity field (b)..	23
Figure 4.5 Velocity field computed on a horizontal section.....	23
Figure 4.6 Temperature field on horizontal section when T=907K and v=10m/s	24
Figure 4.7 Velocity field on horizontal section (a) and parallel plane to the surface (b)	25
Figure 4.8 The vortex part h^* correlating to receiver angle θ	26
Figure 4.9 Ln (Nu) as function of Ln (Re) plot	27
Figure 4.10 CFD Nu data vs correlation data.....	28
Figure 4.11 Wind direction description	29
Figure 4.12 Velocity fields: $\pi/6$ for (a), $\pi/3$ for (b), $\pi/2$ for (c), $2\pi/3$ for (d), $5\pi/6$ for (e), π for (f) and 0 for (g).....	30
Figure 4.13 Velocity field on horizontal section and parallel plane to the surface at 30°	31
Figure 4.14 Velocity field on horizontal section and parallel plane to the surface at 60°	32
Figure 4.15 Velocity field on horizontal section and parallel plane to the surface at 90°	33
Figure 4.16 Velocity field on horizontal section and parallel plane to the surface at 120°	34
Figure 4.17 Velocity field on horizontal section and parallel plane to the surface at 150°	35
Figure 4.18 Velocity field on horizontal section and parallel plane to the surface at 180°	36
Figure 4.19 Display for velocity fields of parallel section.....	37
Figure 4.20 Nu trend for directional wind when T=907K.....	38

Figure 4.21 Nu trend at different temperature at $\pi/6$	39
Figure 4.22 Nu trend for directional wind when $v=5\text{m/s}$	40
Figure 4.23 Nu polar plot for $v=5\text{m/s}$	40
Figure 4.24 Ln (Nu) as function of Ln (Re) plot for different incidence angles	41
Figure 4.25 Distribution of front region and back region	41
Figure 4.26 Analyzed incidence angles grouping	42
Figure 4.27 Ln (Nu) as function of Ln (Re) plot for front region.....	42
Figure 4.28 Ln (Nu) as function of Ln (Re) plot for back region	43
Figure 5.1 Velocity fields:1 for Case 1, 2 for Case 2, 3 for Case 3 and 4 for Case 4.....	46

List of tables

Table 1.1 Jemalong receiver geometry parameters.....	5
Table 2.1 Boundary conditions adopted in the simulations, according to the colors shown in Figure 2.2.....	8
Table 2.2 parameters nominal values	10
Table 3.1 Nusselt number and intermediate data for free convection.....	18
Table 4.1 Boundary conditions when there is wind.....	21
Table 4.2 Pure forced convection Nu from simulations	27
Table 4.3 Directional characteristic length.....	38
Table 5.1 Random simulation parameters setting	45
Table 5.2 Comparison of HTC and <i>Numixed</i>	48

NOMENCLATURE

A	Area, m^2
g	Acceleration due to Earth's gravity
Gr	Grashof number
h^*	Vortex part, m
H	Height of the surface, m
HTC	Heat transfer coefficient
l	Notch length
L	Characteristic length, m
Nu	Nusselt number
P_r	Prandtl number
Q_{conv}	Convection heat losses, W
Ra	Rayleigh number
Re	Reynolds number
T	Temperature, K
u	Flow speed, m/s
W	Width of the surface, m

Greek

α	Constant in Eq. (3)
β	Constant in Eq. (3), coefficient of thermal expansion in Eq. (6)
γ	Constant in Eq. (4)
ν	Kinematic viscosity, m^2s^{-1}
ρ	Density, kg/m^3
η	Constant in Eq. (4)
θ	Receiver angle, rad
μ	Dynamic viscosity, Pa • s

subscripts

air	Environmental temperature, K
conv	Convective heat transfer
f	Forced convection
film	Film temperature, $(T_{air} + T_w)/2$, K
forc	Forced convection

n	Natural convection
mixed	Mixed convection
nat	Natural convection
w	Wall or surface

CHAPTER ONE

INTRODUCTION

1.1 CSP and central tower receivers

Concentrated solar power, abbreviated as CSP, is a system that uses solar power as the resource to generate electricity by collecting sunlight through a considerable number of mirrors or lenses and then focus it onto a receiver.

There has been a blowout growth of worldwide CSP capacity since 2009 and several large plants have been completed in recent years for some developing countries. Also, it has been predicted by some international agencies that by 2050 the concentrated solar power will take up to quarter of the world's energy.^[1]

Comparing to traditional energy sources like fossil fuel, CSP is much more environmentally friendly. Furthermore, it is dispatchable like natural gas and deliver power on demand that although CSP makes solar electricity by harvesting sunlight like PV, it operates more like a conventional power plant. The power block works the same as any other thermal energy power station.^[2]

There are mainly four optical types of concentrating solar power: parabolic trough, dish, concentrating linear Fresnel reflector, and solar power tower, in which parabolic trough (PT) is the earliest and the most developed CSP technology while solar power tower is the fastest growing type.^[3] There are at least 9 new solar power towers that have been completed in the latest 5 years around the world.^[4]

Power tower or central receiver systems use sun-tracking mirrors called heliostats to focus sunlight onto a receiver at the top of a tower. This point focus type leads to a more bigger concentration ratio and as a result, a much higher temperature of the radiated surface of the receiver. The energy that has been absorbed is going to be transferred to a heat transfer fluid which is then be used during the process and at the other side of the circle turbine-generator is producing electricity.^[4]

1.2 The issue of efficiency

According to (Behar et al., 2013)^[4], the efficiency of central receiver is around 16,17% at that time and a significant improvement on efficiency can be made that the relative rise of efficiency can reach to 40%-65%. This great potential to increase the efficiency makes central tower system a rising star that recently many companies are building power plants using central tower technology.

The overall efficiency is combined with the receiver efficiency and the system conversion efficiency. The working temperature has its influence on efficiency that a high temperature can increase receiver efficiency but decrease overall one which is dependent on receiver design, which in turn depends on heat transfer fluid. By using a good transfer fluid, an open-type receiver design with small area and moderate outer temperature can be achieved. ^[6]It can be said that transfer fluid is playing a very important role in deciding the receiver design including the type of the receiver which has influence on the efficiency.

Several materials have been investigated as heat transfer fluids (HTFs) such as liquid sodium, steam, nitrate molten salts and air. Among all, molten salts are better options because of their superior heat transfer and energy storage capabilities. ^[6]With its high conductivity and a reasonable density and a high boiling point, liquid sodium has presented a good combination of characteristics for advanced CSP.^[8]

According to some literatures, liquid sodium seems to have the advantages as a heat transfer fluid not only because of the wider operating temperature range but also for the much higher thermal conductivity. ^[9]

1.3 The Jemalong receiver and previous attempts to evaluate losses



Figure 1.1 Jemalong solar thermal station: overview.

Completed in 2017, a sodium-cooled CSP plant in Jemalong (Australia) Solar Thermal Station was developed by Vast Solar with its five array-modules concentrate solar radiation on a thermal receiver tower 27-meters height, see Figure 1.1. This receiver is billboard type and is shown in Figure 1.2. The five modules are connected to the central thermal energy storage tank, from which the stored thermal energy is transformed through a steam generator to make steam for a 1.1MWe turbine and electricity generator. Jemalong CSP Pilot Plant is one of the first in the world to deploy the MACCSol air cooled condenser which is specifically designed for the plants in water-scarce areas. ^[10]



Figure 1.2 Jemalong solar thermal station: solar receiver on one tower.

The receiver geometry was simplified in a CAD model as showed in Figure 1.3. The receiver is billboard-type with two lateral wings and overhang, the surface has an inclination of 20° with respect to the direction perpendicular to the ground. The width and the height of the irradiated surface have been marked in this Figure and the other geometry parameters are presented in Table 1.1.

This specific plant has been used as a reference plant and this work is a further step based on the achievement by Marco Lanzani from Politecnico di Milano^[11]. During his work, the model had been used in commercial CFD software STAR-CCM+ to simulate the convective heat losses towards the surrounding environment. Considering the formula proposed in Sandia report^[15], forced convection results were derived from mixed and natural convection, based on data derived from the CFD simulations. In those simulations, different parameters were set such as surface temperatures, wind intensity and air directions. Finally, several correlation procedures were carried out based on Nusselt number with dependence on Rayleigh, Reynolds and Prandtl numbers so that the convective heat losses could be predicted.

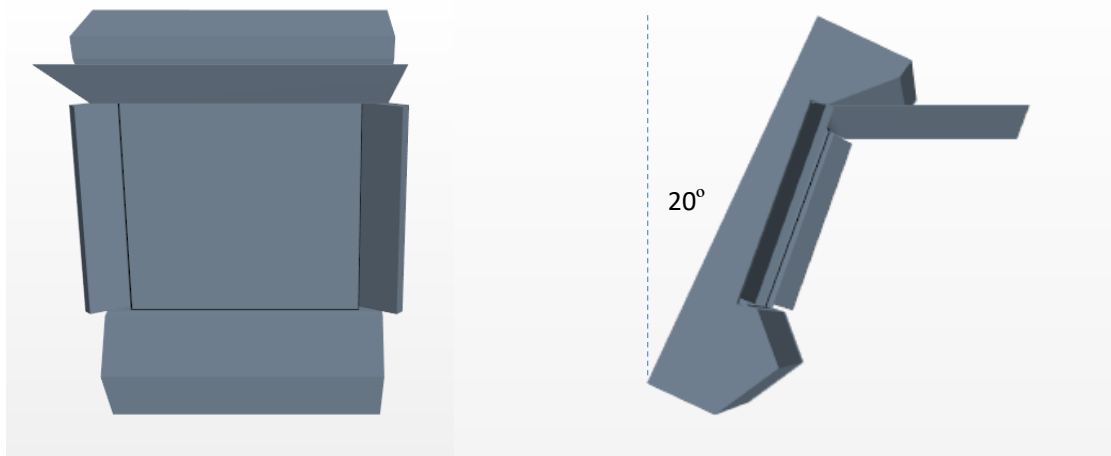


Figure 1.3 Jemalong solar receiver: simplified CAD model

Table 1.1 Jemalong receiver geometry parameters

Hot surface height [m]	1.56
Hot surface width [m]	1.67
Later wings width [m]	0.30
Later wings angle	30°
Overhang length [m]	1.45

Many factors can influence convective heat transfer. First to be mentioned is the receiver design which can be a cylinder, external or a cavity-type or like what we analyze in this work-

a flat plate. But with the lateral wings and overhang it is more likely to be a semi cavity one. Other factors include operating conditions and environmental conditions that these two together will make a huge impact on heat transfer energy losses.

1.4 Aim of the work

This work is based on the previous work but using a different approach. Pure forced convection data are computed in simulations with gravity off and, after combining with natural convection, mixed convection is obtained. Then the results can be compared to the empirical correlation available in Sandia report^[15]. Besides, this work will be able to give a comprehensive view of the thermal and dynamic characteristics and behavior around the receiver as well as temperature and vector fields that are studied under different parameters. Hopefully, at the end, what has been presented here could be a reference for the further study.

This work is going to be divided into three parts to present the results: natural convection, forced convection due to the wind effect and mixed convection. A validation of the final recipe is also carried out on an independent set of simulations.

CHAPTER TWO

COMPUTATIONAL MODEL

2.1 Computational domain

As showed in Figure 2.1, a certain volume is included around the receiver as computational domain in CFD thus it is a proper way to describe the environment nearby the receiver in simulations. It has been set to be a volume of dodecagon because it is more convenient to set the inlet and outlet boundary conditions for the later section which studies the external behavior of air and the heat losses when the receiver is under different wind direction and intensity.

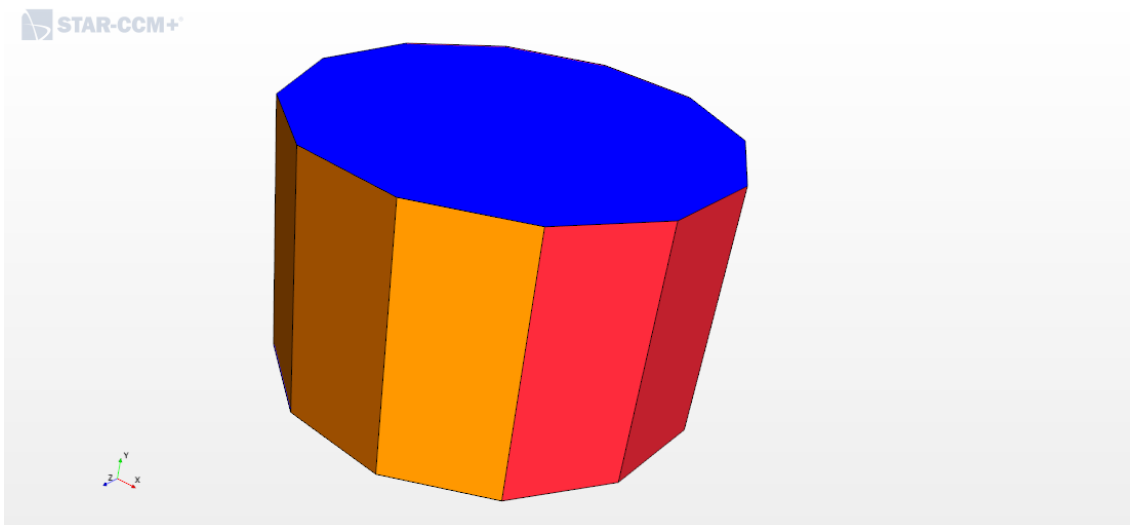


Figure 2.1 Computational CFD domain adopted in the present study.

In Figure 2.2 it shows the situation when the wind comes from 30° with respect to the frontal position of the surface. The setup of boundary conditions can be referred to Table 2.1.

Table 2.1 Boundary conditions adopted in the simulations, according to the colors shown in Figure 2.2

Color	Boundary condition
red	Velocity inlet
orange	Pressure outlet
blue	symmetry

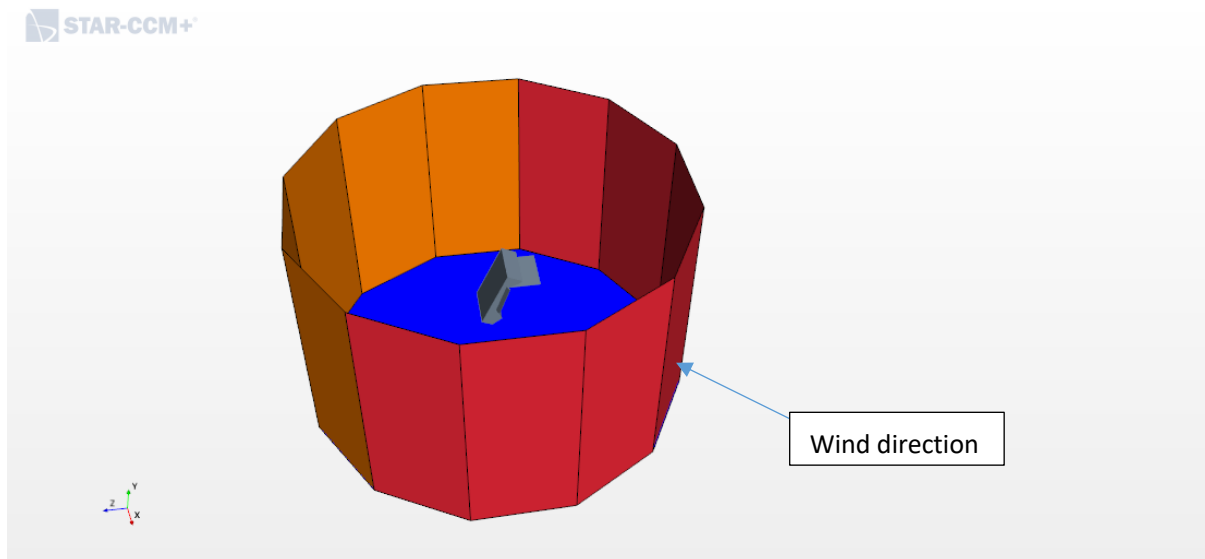


Figure 2.2 Example of the computational CFD domain adopted for the simulations with wind direction of 30°.

2.2 CFD grid

As showed in Figure 2.3 and Figure 2.4, to get sufficient but proper cells number of mesh, the discretization of the computational domain needs to be done and therefore the total volume of the computational domain can be subdivided into three parts that each part hold with different cells' dimension and precision. The detailed grid independent study was performed by M.Lanzani and the same grid recipe is inherited in this work.

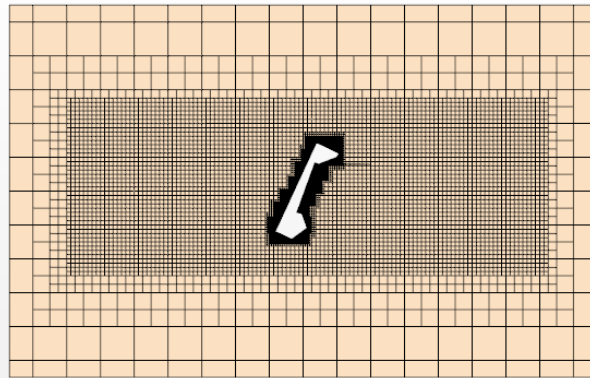


Figure 2.3 Mesh domain, vertical section

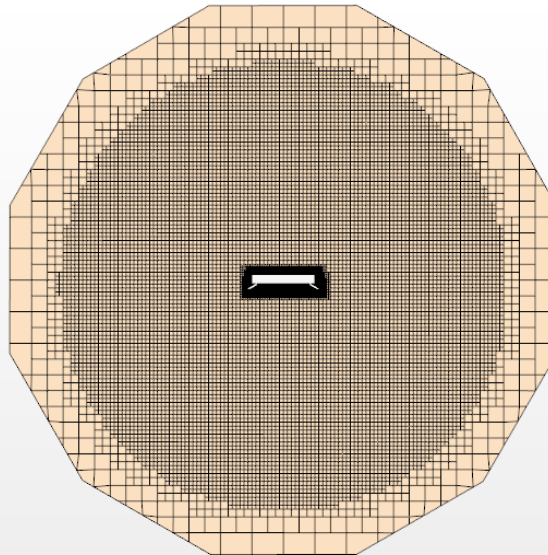


Figure 2.4 Mesh domain, horizontal section

The whole computational domain has been divided into three subdivisions: the outside space, the middle space and the inside space that surrounds the receiver. It is obvious that as it gets nearer to the receiver, the cells dimension is getting smaller because it demands more cells precision within small distance to the receiver surface. But the balance between the total cells number and the cells quality is very crucial. Basically, if the number of the cells is too big it would require more time to resolve so a compromise needs to be done. The best scenario is that with a relatively smaller number of cells, the same accuracy can be achieved. As a result, a

lower computational cost can be acquired.

Other than cells number and cells dimension, there are other parameters that will influence the quality of the mesh which are cells geometry, number of prism layer, prism layer thickness and so on. The sensibility of these parameters on the solution needs to be studied independently before getting the best combination.

2.3 Turbulence closure

Here a 3D steady state RANS-type (Reynolds Averaged Navier-Stokes's equations) model has been chosen which is implemented in the commercial software STAR CCM+. And turbulence type we chose is Shear-Stress Transport (SST) k- ϵ turbulence model because in some study this type of model reproduce validation data well when both natural and forced convection are existing^[12], compared to other models such as k- ϵ , Launder Sharma, etc.

2.4 Simulation setup

The velocities applied in this thesis are 0, 5, 10 and 15 m/s, they are chosen referring to the weather data recorded by Australian Government – Bureau of Meteorology.^[13] On the hot surface of the receiver, a uniform temperature boundary condition is applied in CFD simulations while adiabatic condition is applied for the other surfaces of the receiver. The temperatures are chosen to be 502, 602, 702, 802, 907 and 1002 kelvin which are between the melting point and boiling point of sodium. All the combinations are presented in Table 2.2, there are 168 combinations in total considering all the nominal values of wind direction, surface temperature and wind speed.

Table 2.2 parameters nominal values

Wind directions θ	$\theta=0, \pi/6, \pi/3, \pi/2, 2\pi/3, 5\pi/6, \pi$
Temperature T	T=502K, 602K, 702K, 802K, 907K, 1002K
Wind speed V	V=0, 5, 10, 15m/s

CHAPTER THREE

ANALYSIS OF FREE CONVECTION LOSSES

There are so many relevant heat transfer correlations that are available in the literature, especially from Sandia report^[15] that contains the information for the vertical plate which is similar with the case analyzing here. Therefore, this chapter is going to reveal an effective and comparable way to express heat transfer correlations for free convection situation along with the computed results of main features from the CFD simulations.

3.1 Convective heat transfer correlation

The analysis of convective losses begins with the following formula that is common knowledge in thermodynamics.

The equation to estimate the total convective energy losses can be expressed as in Eq. (1):

$$Q_{conv} = HTC * A * (T_w - T_{air}) \quad (1)$$

In (1), Q_{conv} is the total convection heat losses from the receiver to the environment [Watt], HTC is the average heat transfer coefficient for the hot receiver [$W/(m^2K)$], A is the hot surface area and T_w is the receiver surface temperature and T_{air} is the ambient temperature in standard conditions.

As Q_{conv} can be computed and acquired from CFD simulations, the area of the surface and the temperatures are known for they are input parameters, the average heat transfer coefficient can be obtained.

A dimensionless term used to be as the heat transfer correlation is Nusselt number that can

be expressed as in Eq. (2):

$$Nu = HTC * L/k \quad (2)$$

In (2), Nu is the Nusselt number, L represents the characteristic length that will be discussed further in the next subsection and k is the thermal conductivity of the fluid. Combining this formula with Eq. (1) then Nusselt number is successfully derived. The procedure to get Nusselt number from the raw data obtained in the CFD simulations is presented in Figure 3.1 and this process would also be applied in the following chapters when needed.

A Nusselt number represents the ratio of convective to conductive heat transfer in a fluid. It has been proven^[14] that Nusselt number is dependent on many other dimensionless parameters such as Reynolds number, Prandtl number, Grashof number and Rayleigh number. While in this chapter, for a better description, the final form of the correlation should be Rayleigh number dependency while in the following chapters, it may show a different dependency on other parameters. The comprehensive and more profound impact of surface temperature, wind intensity and wind direction on this correlation will be delivered in the following content. As a result, the relation between engineering and environmental variables and thermodynamics characteristics has been constructed.

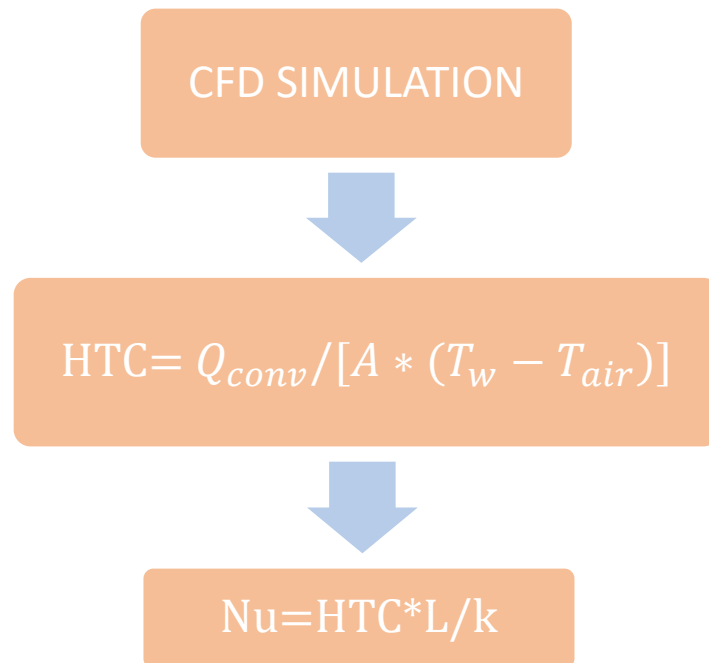


Figure 3.1 Procedure adopted in this work to compute the Nusselt number from CFD results

3.2 Characteristic lengths for the heat transfer

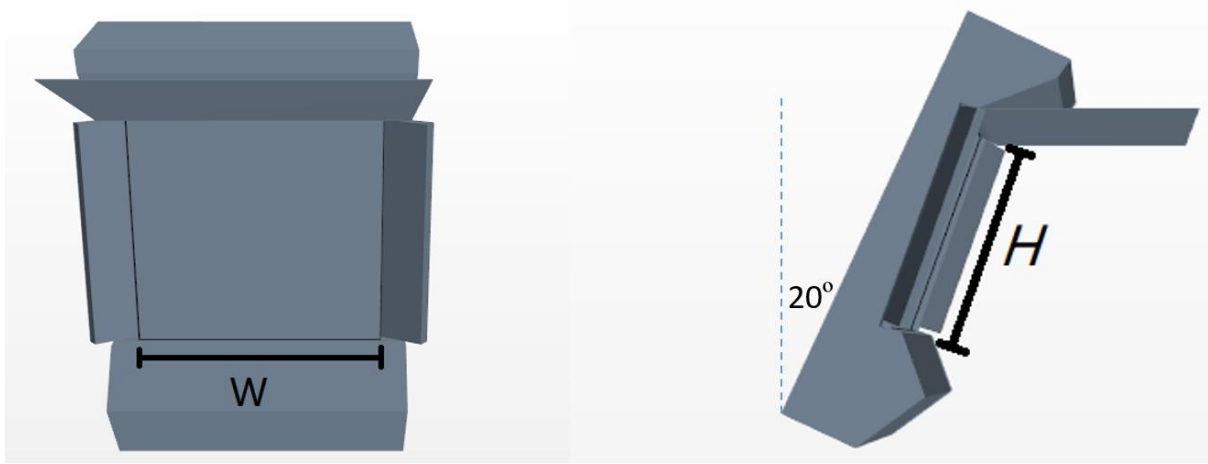


Figure 3.2 Main dimensions for expressing the characteristic length. W is defined as the width of the surface that will be used in wind direction problem., H as the height of the surface that will be used in free convection analysis and in wind effect analysis.

As shown for Eq. (2) in the previous section, the characteristic length has been used as a quantity in the definition of Nusselt number. According to Siebers' studies^{[15][16]}, correlation equations are expressed in Eq. (3) and Eq. (4):

$$Nu_{nat} = \alpha Ra^\beta \quad (3)$$

$$Nu_{forc} = \gamma Re^\eta Pr^{1/3} \quad (4)$$

In (3), Rayleigh number Ra is defined as in Eq. (5):

$$Ra = G_r P_r \quad (5)$$

In (5), P_r is Prandtl number and Grashof number G_r for vertical flat plates is defined as in Eq.(6):

$$G_r = \frac{g\beta(T_s - T_{air})L^3}{\nu^2} \quad (6)$$

In (6), β is coefficient of thermal expansion, ν is kinematic viscosity, g is acceleration due to Earth's gravity, T_s and T_{air} are temperatures for the surface and the air respectively, L is the characteristic length. β and ν are evaluated at the film temperature of the fluid that is defined

as in Eq. (7):

$$T_{film} = \frac{T_s + T_{air}}{2} \quad (7)$$

In (4), Reynolds number Re is defined as in Eq. (8):

$$Re = \frac{\rho u L}{\mu} \quad (8)$$

In (8), ρ is the density of the fluid, u is the flow speed, μ is the dynamic viscosity of the fluid and L is the characteristic length.

It can be noticed that characteristic length is showing in the definitions for Reynolds number and Grashof number both of which are important reference numbers that will greatly influence the final correlation result. The appropriate choice of characteristic length is crucial throughout the analyzing procedure.

A characteristic length is usually chosen as the dimension along the direction of the fluid. In this case, the characteristic length for natural convection should be assumed as H that indicated the height of the receiver surface, see Figure 3.2, because the heated air near the hot surface is prone to go up that the moving direction is along the height of the plate. This assumption will be confirmed by the features of the computed results that will be showed in the next part.

3.3 Main features of the computed results

To confirm the characteristic length for natural convection, the temperature fields and velocity fields are presented down below in Figure 3.3.

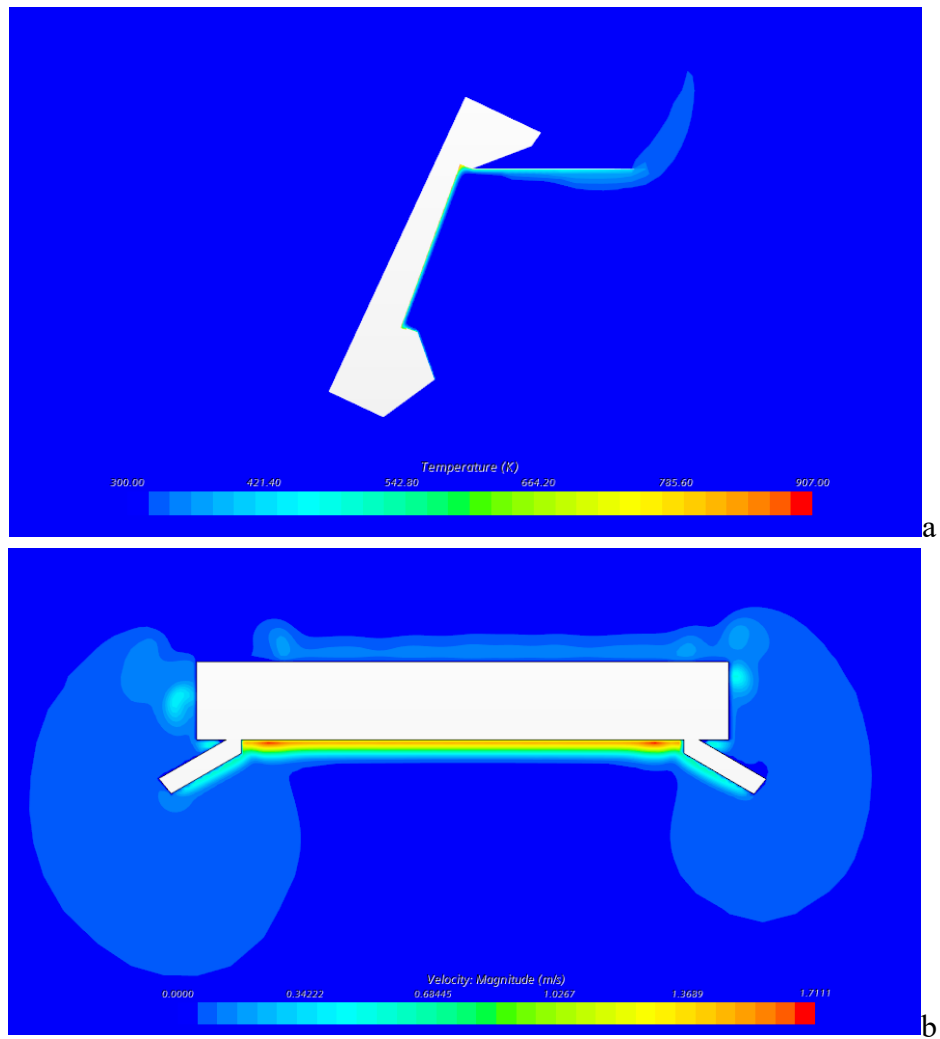


Figure 3.3 Temperature fields for natural convection when $T=907\text{K}$. vertical (a) and horizontal (b) section views

Observing the boundary layer of temperature, the characteristic length should mainly depend on the direction along the hot surface. To better have an observation on the boundary layer, the zoomed Figure 3.4 can be referred to.

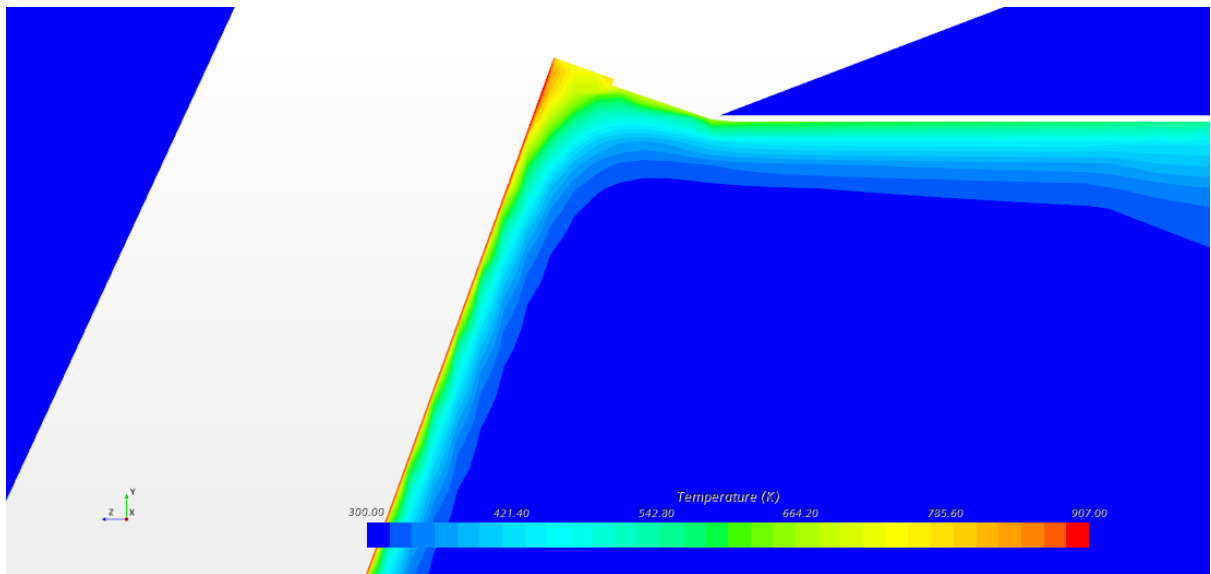


Figure 3.4 Vertical temperature fields zoomed near the edge of the hot surface

After delimiting the area range for the characteristic length, the velocity fields are now used to find out the movement of the air near the hot surface, see Figure 3.5.

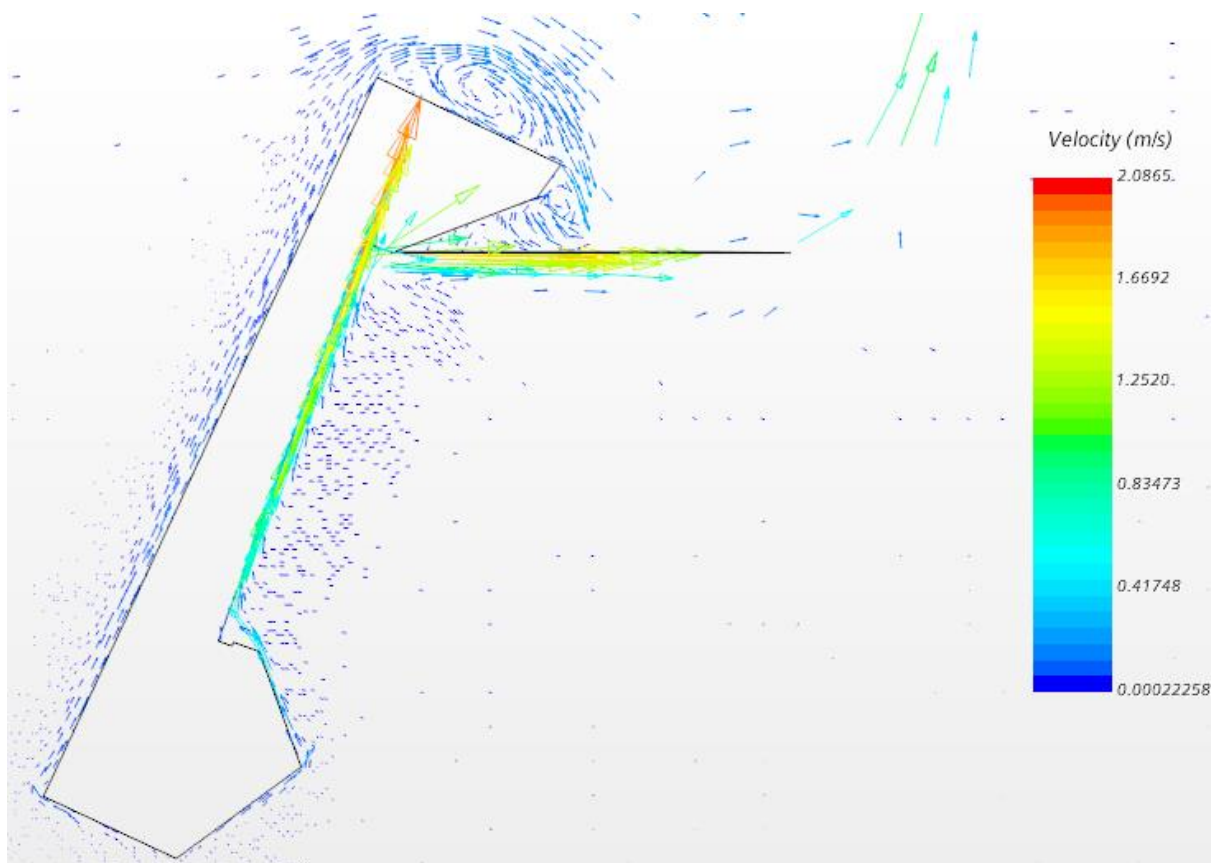


Figure 3.5 Vertical section velocity vector field for natural convection when $T=907K$

As already been assumed in the previous section, the air near the receiver is heated up by the

hot surface which drive the air from the bottom to the top of the receiver until it reaches the overhang and then along its direction. This demonstrate that the characteristic length is the height of the hot surface. Officially here comes the conclusion of the characteristic length for the natural convection that

$$L_{nat} = H \quad (9)$$

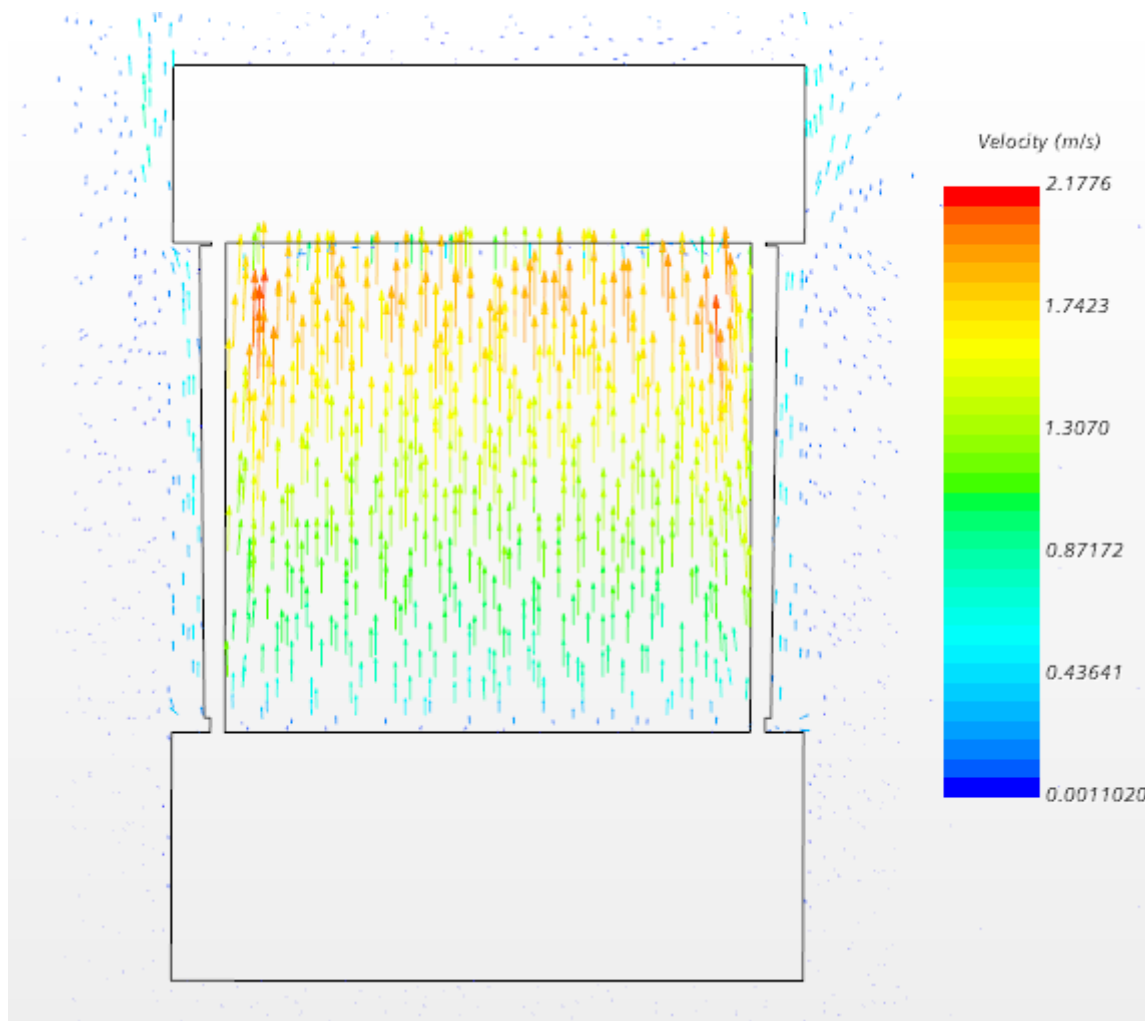


Figure 3.6 Velocity vector field from the section parallel to the hot surface

From another point of view as presented in Figure 3.6, it is more convenient to observe the movement of the air from the bottom to the top of the surface. Combining with the previous vertical velocity field, a more comprehensive view regarding the fluid movement is obtained.

3.4 From HTC to Nu correlation

The correlation developing procedure starts from the calculations for Nusselt number

according to the procedure presented in Figure 3.1. The free convection heat flux has been recorded after the simulation and the corresponding Nu_{nat} is presented in Table 3.1 for each temperature.

Table 3.1 Nusselt number and intermediate data for free convection

T_{surf} [K]	HTC	Nu_{nat}	Ra
502	4.28	202	1.96E+10
602	4.71	201	1.72E+10
702	5.05	198	1.44E+10
802	5.32	193	1.18E+10
907	5.56	188	9.65E+09
1002	5.75	183	7.99E+09

For a flat plate in free convection, the Nusselt number usually can be expressed as a dependency on Ra number as in Eq. (3) that has been mentioned before:

$$Nu_{nat} = \alpha Ra^\beta \quad (3)$$

To get the values of α and β in Eq. (3), a logarithmic fit is being conducted as shown in Eq. (10):

$$Nu_{nat} = \alpha Ra^\beta$$

↓

$$\ln Nu_{nat} = \ln \alpha + \beta \ln Ra \quad (10)$$

After substitute Nu_{nat} from Table 3.1 and Ra that has been calculated and we can expect a linear fit which has been showed in Figure 3.7.

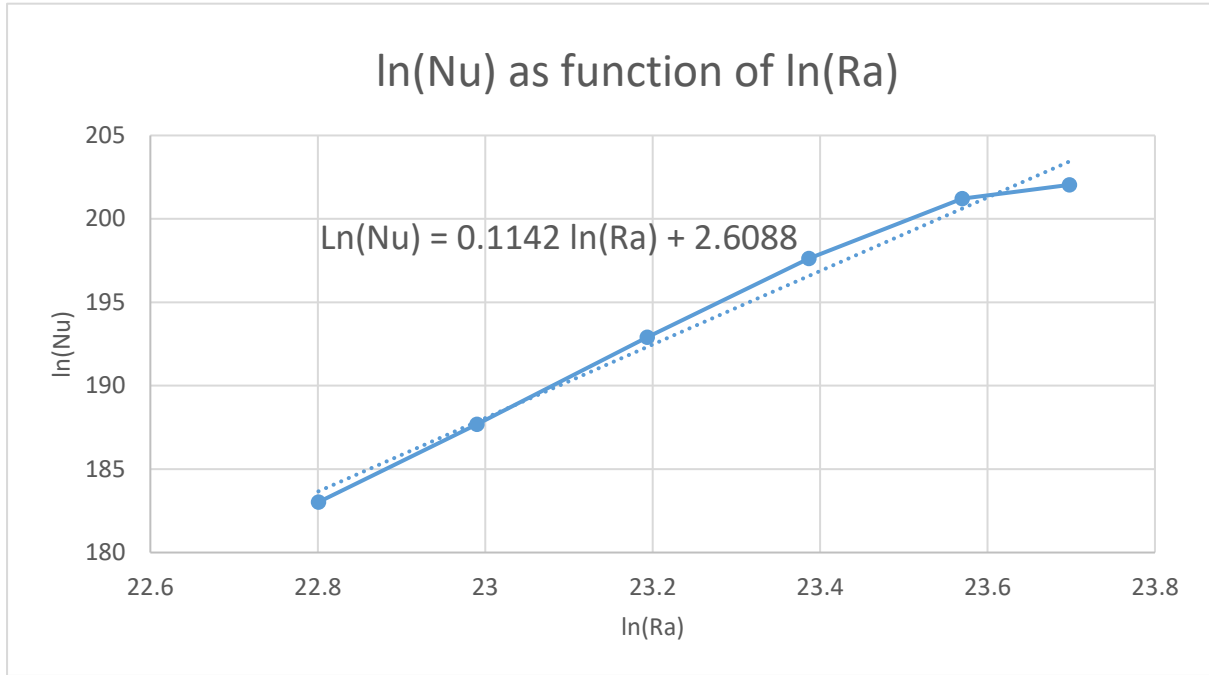


Figure 3.7 Ln (Nu) as function of ln (Ra) plot for the free convection computed results

Eq. (10) indicated that there is supposed to be a linear relationship between $\ln(Nu_{nat})$ and $\ln(Ra)$. A better linear fit represents a better accuracy for the Nu correlations deriving from linear interpolation of the computed values from CFD. In Figure 3.7, Eq. (10) is showed and α and β have been acquired:

$$\alpha = 13.6$$

$$\beta = 0.114$$

Eq. (3) now can be written as

$$Nu_{nat} = 13.6 Ra^{0.114} \pm 1.01 \quad (11)$$

in which 1.01 represents the standard deviation of the fit.

CHAPTER FOUR

ANALYSIS OF LOSSES DUE TO WIND

Considering the environmental reality for the receiver, other than the situation when there is completely no wind, which is rare condition, the most common condition should be that the receiver is facing the wind from any possible direction that not only natural convection is happening, but also forced convection is playing its role. For simplification, only horizontal wind is analyzed throughout the whole chapter.

4.1 Analysis of forced convection when facing frontal wind

Right at the beginning of this wind problem analysis, the frontal direction is going to be analyzed: symmetric with respect to the receiver and parallel to the ground, based on which, the further analysis for other directions can be made.

4.1.1 Boundary conditions and simulation setup

As showed in Figure 4.1, the boundary conditions' setting for forced convection is different from the one for free convection that the red side face represent velocity inlet and the orange side faces are to be set as pressure outlet. The wind intensity equals to 5, 10, 15 m/s, respectively. All the details of boundary conditions can be referred to Table 4.1.

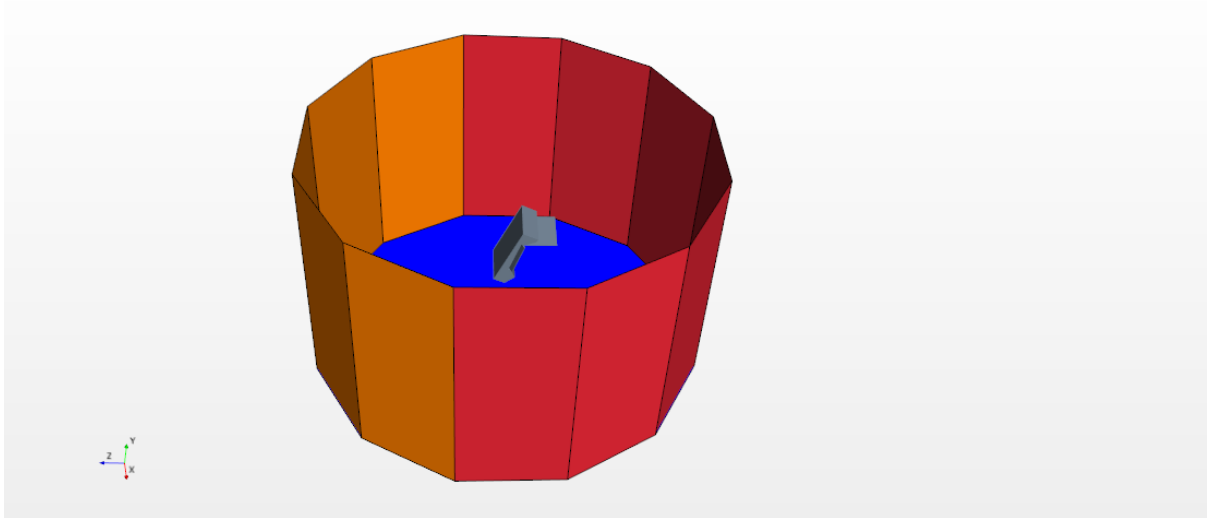


Figure 4.1 Computational domain and boundary conditions when wind comes from frontal direction

There is a crucial change in the model selecting that the gravity has been turned off in CFD simulations so that the buoyant effect can be killed, as a result we get rid of the free convection and the pure forced convection is going to be simulated.

Table 4.1 Boundary conditions when there is wind

<i>Color</i>	<i>Boundary condition</i>	
<i>red</i>	Velocity inlet	NOTE: As the wind direction is changing, the inlet and outlet boundary conditions need to be reassigned. The relative position between the receiver and the mid-position of velocity inlet decides the angle for the wind.
<i>orange</i>	Pressure outlet	
<i>blue</i>	symmetry	

4.1.2 Main features of computed results

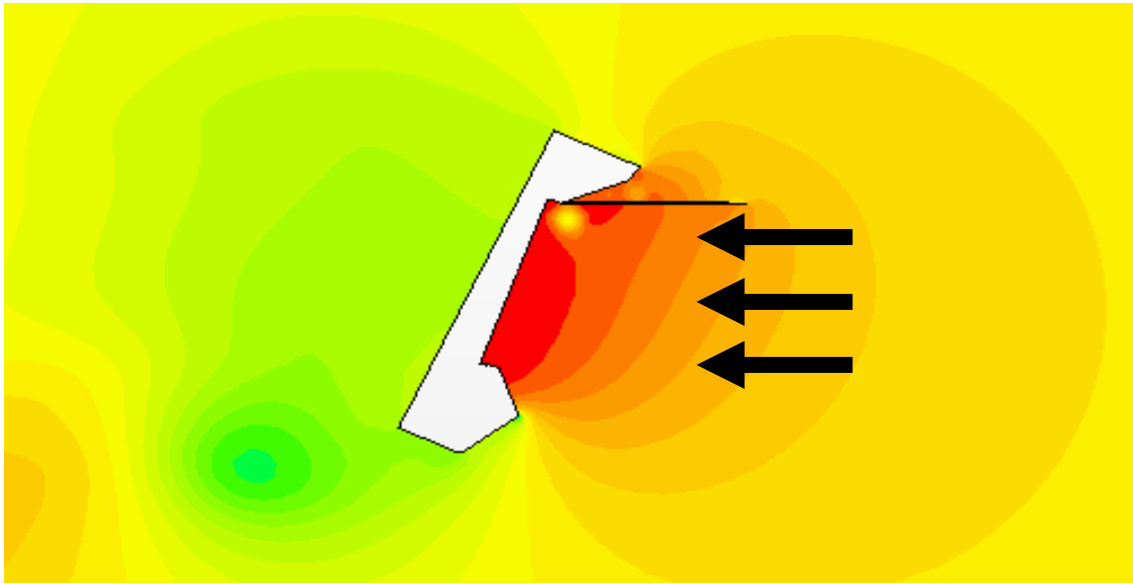


Figure 4.2 Pressure field computed on a vertical section when $T=907\text{K}$ and $v=5\text{m/s}$

In Figure 4.2, the black arrows represent the wind direction, it has showed that the area in front of the hot surface of the receiver is in high pressure because of the wind while at the back of the receiver the pressure is negative because of the turbulent fluid which can be better seen from velocity field showed in Figure 4.3.

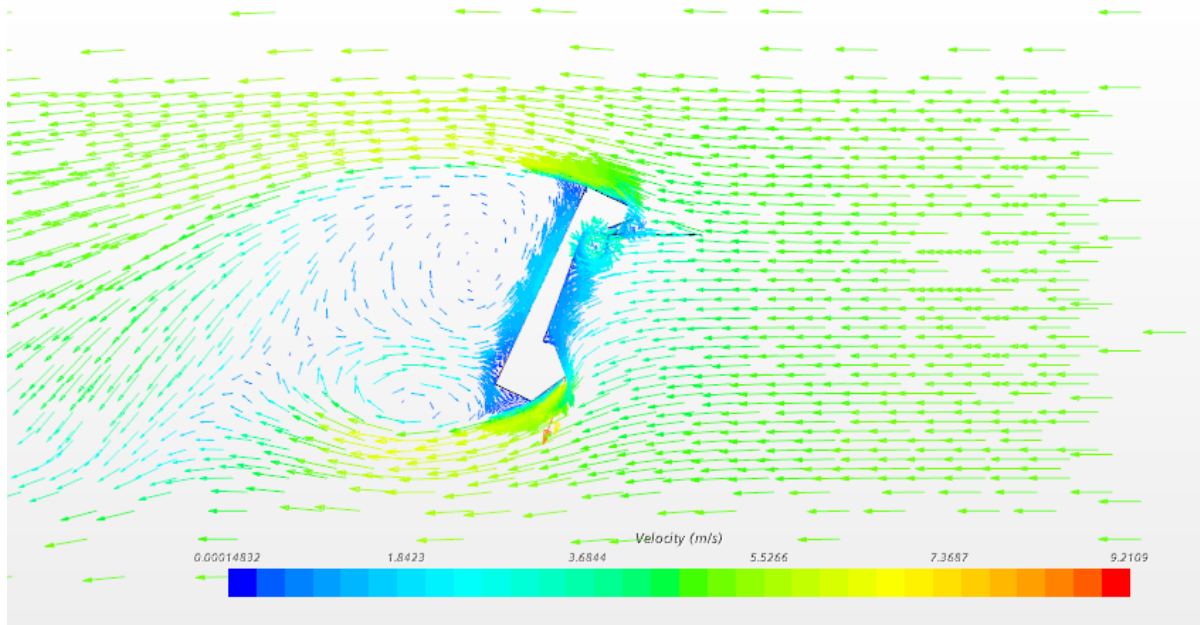


Figure 4.3 Velocity field computed when $T=907\text{K}$, $v=5\text{m/s}$, frontal wind, lateral view

We can notice that below the connection part of the overhang and the receiver there is a

small area of pressure reduction because of the vortex that is formed because of the corner stagnation phenomena that can be better observed from the zoomed Figure 4.4.

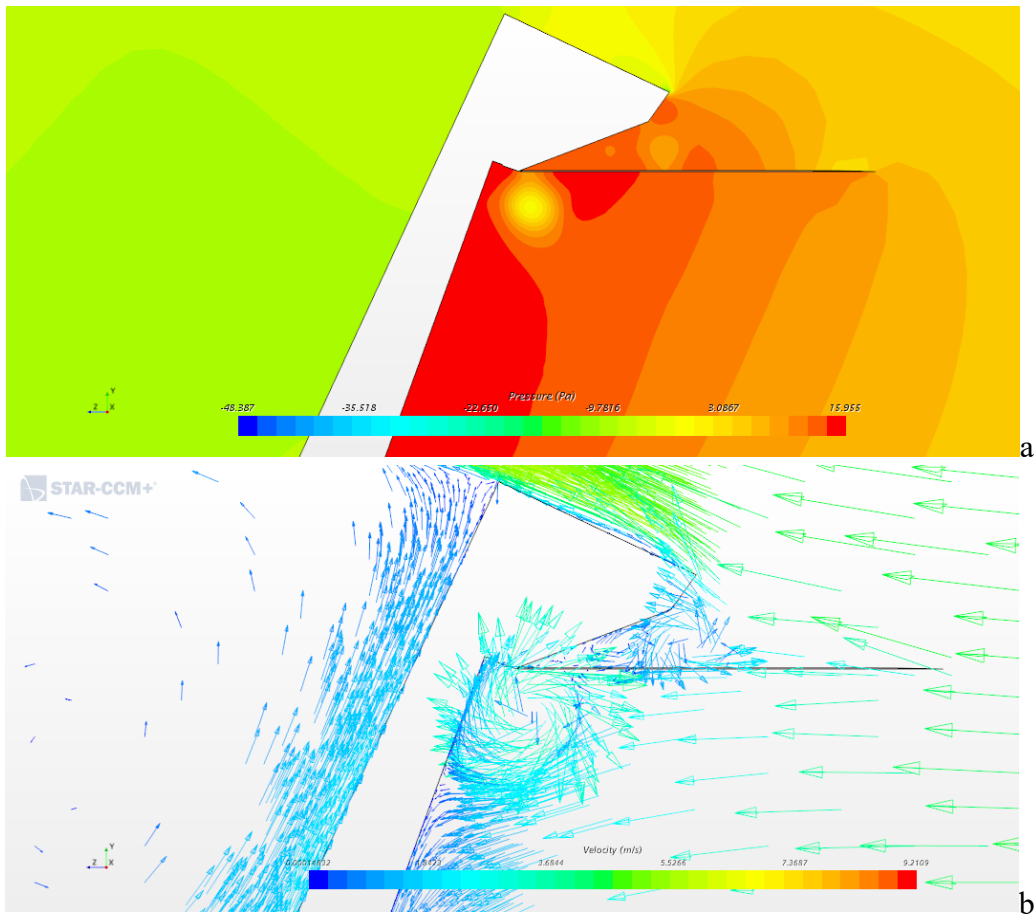


Figure 4.4 Corner stagnation phenomena, zoomed pressure field (a) and zoomed velocity field (b)

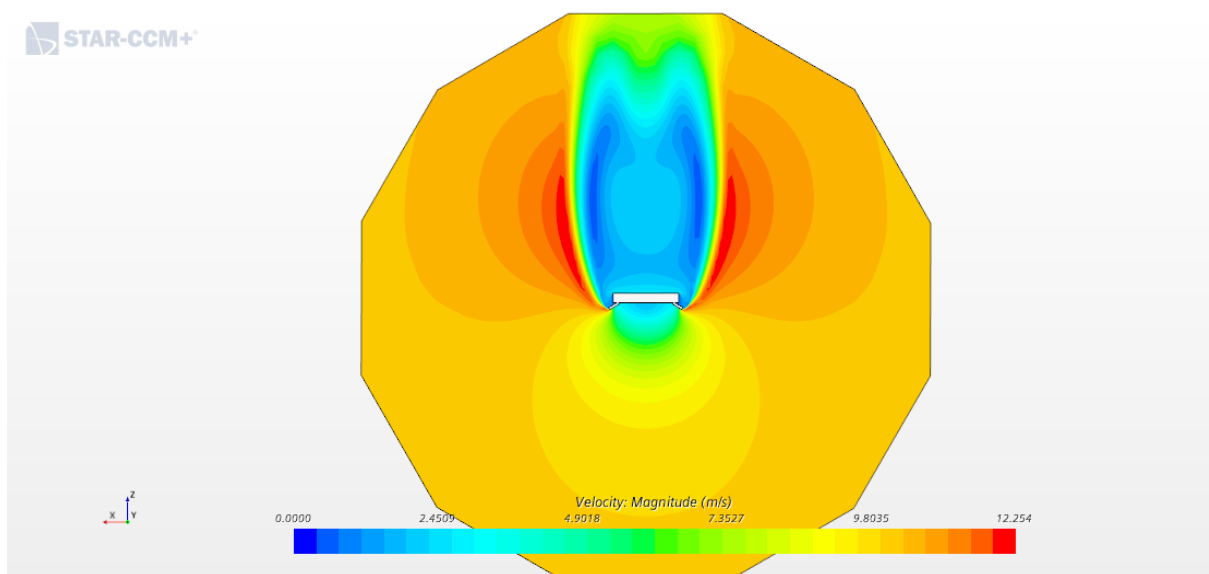


Figure 4.5 Velocity field computed on a horizontal section

From Figure 4.5 we can notice that the lateral wings behave as barriers which makes the receiver like a semi-cavity one.

It can be imagined that as the air flow reaches the hot surface, it has been divided into two separate and symmetric branches. Before they leave the receiver, it is very important to identify the paths of the air stream through which the characteristic length can be acquired. In later section this specific problem will be focused on.

4.1.3 Evaluation of characteristic length

Before doing the procedure of getting convective heat transfer correlation, the characteristic length needs to be confirmed.

In chapter three, the characteristic length for free convection has been demonstrated to be the height of the hot surface while here for forced convection, under the influence of wind, the trend of the airstream must have been differed.

To begin with, the temperature map is showed in Figure 4.6. The boundary layers are getting thinner comparing to the free convection because of the wind effect. And the scope range for the characteristic length still goes under the dimensions of the surface.

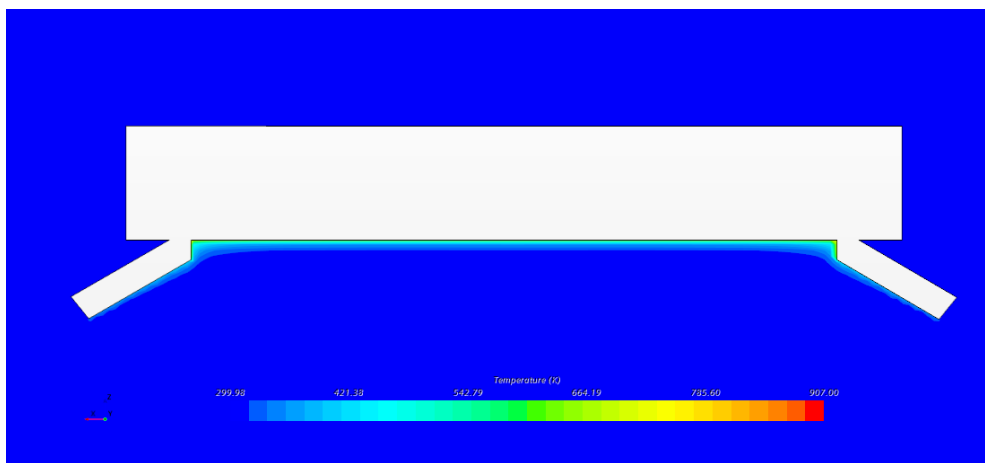


Figure 4.6 Temperature field on horizontal section when $T=907\text{K}$ and $v=10\text{m/s}$

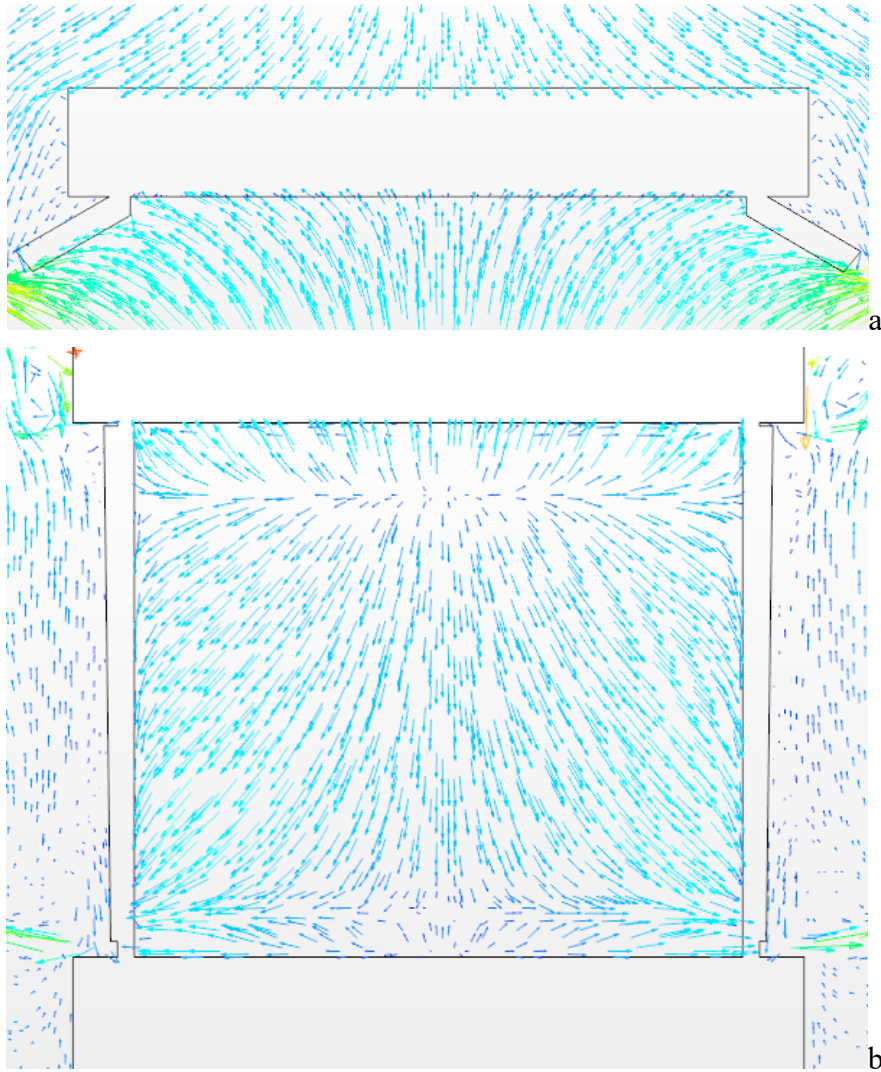


Figure 4.7 Velocity field on horizontal section (a) and parallel plane to the surface (b)

Other than two vortices on the top edge and the bottom edge (see Figure 4.7), the air fluid is mainly showing a movement combining descending and walking aside. The characteristic length for forced convection should be considered similar as in the diagonal direction as defined in Eq. (12):

$$L_c = \sqrt{H^2 + \left(\frac{W}{2}\right)^2} \quad (12)$$

Eq. (12) for characteristic length is an attempt definition supposing that along the dimension of height, the length portion of vortex to H is small. If this presumption is confirmed, then the way to obtain the characteristic length through Eq. (12) will be established.

As presented in Figure 4.8, the slot width and the receiver placing angle are two parameters

that will affect the possible length portion of vortex.

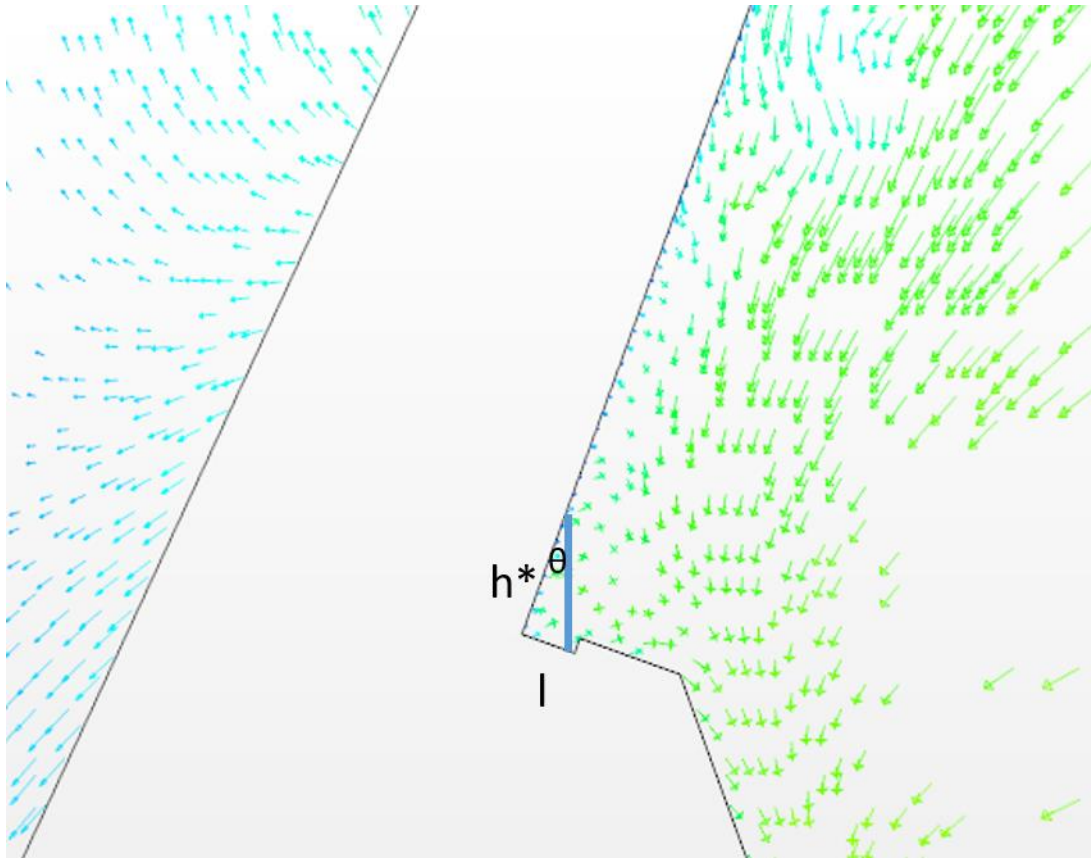


Figure 4.8 The vortex part h^* correlating to receiver angle θ

The relationship between vortex part h^* and θ can be expressed as in Eq. (13):

$$h^* = l/\tan\theta \quad (13)$$

After simple calculating, h^* is supposed to be around 0.137m which is relatively small with respect to H that is 1.56m.

4.1.4 From HTC to Nu correlation

The characteristic length has been figured out in the previous section. The process to get Nusselt number is the same as what been done in chapter three. In Table 4.2, the Nu number getting from the CFD results are presented.

Table 4.2 Pure forced convection Nu from simulations

$v(\text{m/s})/T_{film}(\text{K})$	400	450	500	550	602.5	650
5	367	340	320	303	288	276
10	558	581	534	443	420	402
15	731	656	603	564	531	507

All the Nu numbers presented here are pure forced convection because the gravity model in the simulation has been switched off.

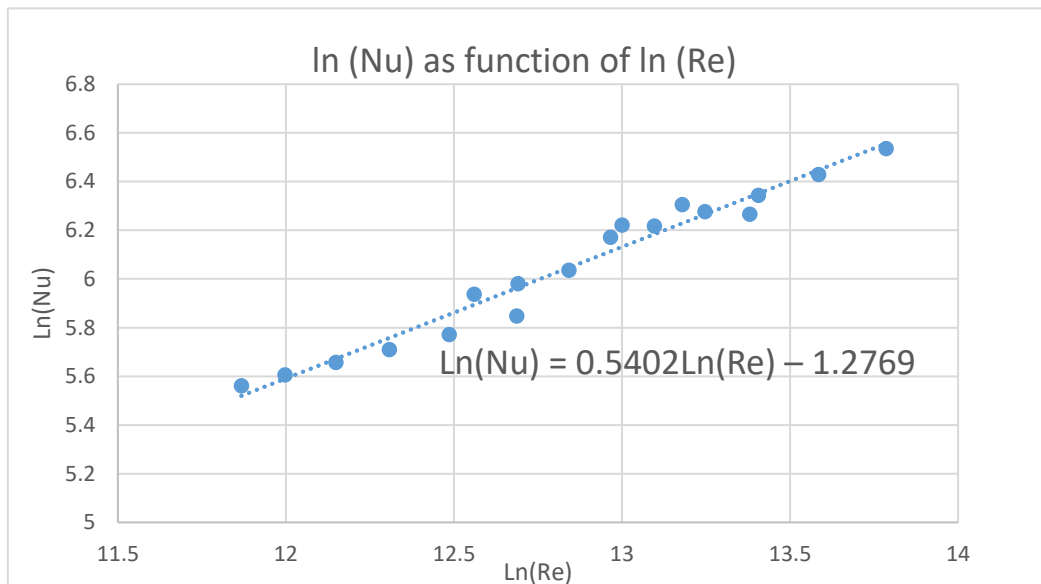


Figure 4.9 Ln (Nu) as function of Ln (Re) plot

Nusselt number for forced convection shows an empirical correlation as a function of Reynolds number and Prandtl number:

$$Nu_{forc} = \gamma Re^n Pr^{1/3} \quad (4)$$

In (4), the fluid properties are evaluated at film temperature. The exponent $1/3$ in Eq. (14) is indicated in Siebers' Sandia report^[15] for a flat plate.

If Eq. (4) is valid, a linear relationship between logarithmic properties for Nusselt number

and Reynolds number is predictable that in Figure 4.9, it is verified as the formula. After using the parameters in the formula, the forced convection Nu correlation is obtained in Eq. (14).

$$Nu_{forc} = 0.479Re^{0.540}Pr^{1/3} \pm 25.7 \quad (14)$$

In (14), the standard deviation of the fit is present at the end.

The comparison between the Nu calculated from CFD simulations and the Nu correlated from Eq. (14) is showed in Figure 4.10.

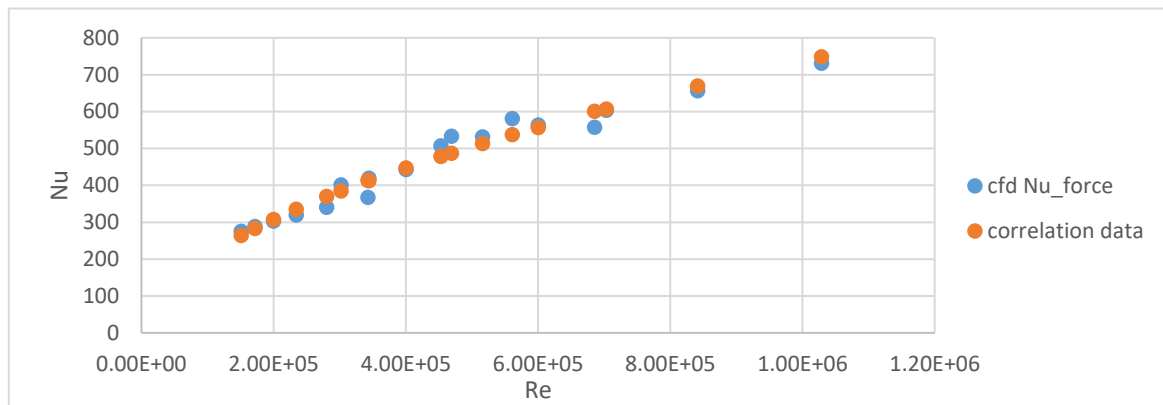


Figure 4.10 CFD Nu data vs correlation data

4.2 Analysis for forced convection when wind is coming from other directions

-wind direction effect

In the previous part, we only focused on the frontal direction. Furthermore, it is necessary to present the situations when the wind comes from other directions. Considering the shape of the computational domain, it is more than convenient to choose the directions that are normal to side faces of the computational domain. Because of its symmetry, only half circle is sufficient for the other one is the same. There are six more wind directions to be studied other than the frontal one (a) as showed in Figure 4.11.

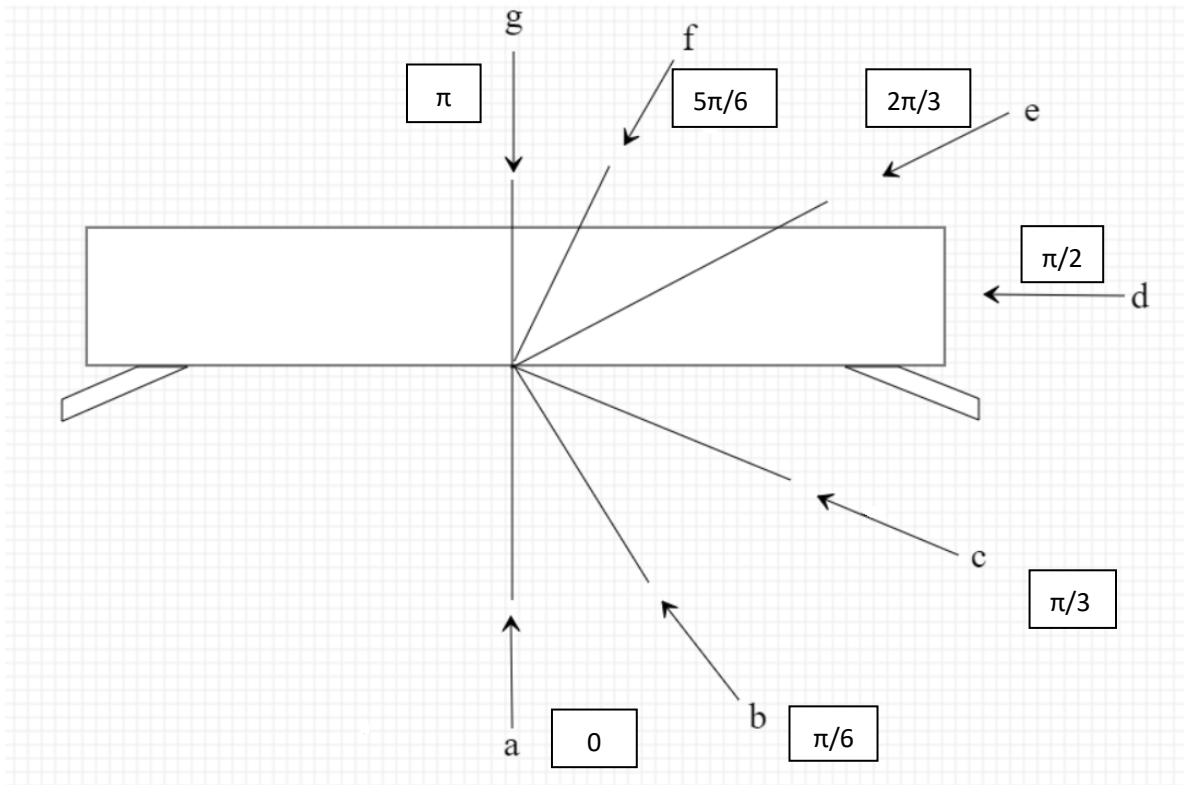


Figure 4.11 Wind direction description

4.2.1 Velocity fields of computed results

The velocity fields are placed in sequence in Figure 4.12. From Case (a) to Case (f) the incidence angle increases from $\pi/6$ to π and Case (g) is the case that has been analyzed in section 4.1 with wind coming from the frontal position. This group of pictures are the results from the condition that the surface temperature equals to 907 K and the wind intensity is 10m/s.

As the wind direction angle increases from frontal position and it does not exceed the region set by the lateral wings, the magnitude of velocity gets higher near the hot surface, especially at the Case (b) when the wind direction is tangential to the lateral wing, majority of the surface is under the influence of wind that carries a relatively high velocity. When the angle gets to 90 degrees, the lateral wing is acting as a barrier that the intensity of the heat transfer between the surface and the air is decreasing significantly. For all the back wind cases, the air is shielded in some level by the receiver body and the relatively lowest velocity in front of the surface is achieved at Case (f) that the wind is coming from straight behind.

Helping to display the status of the turbulence and the formation of the vortex, the velocity vector fields are showed in the next section from which it may reveal the way to figure out the characteristic length.

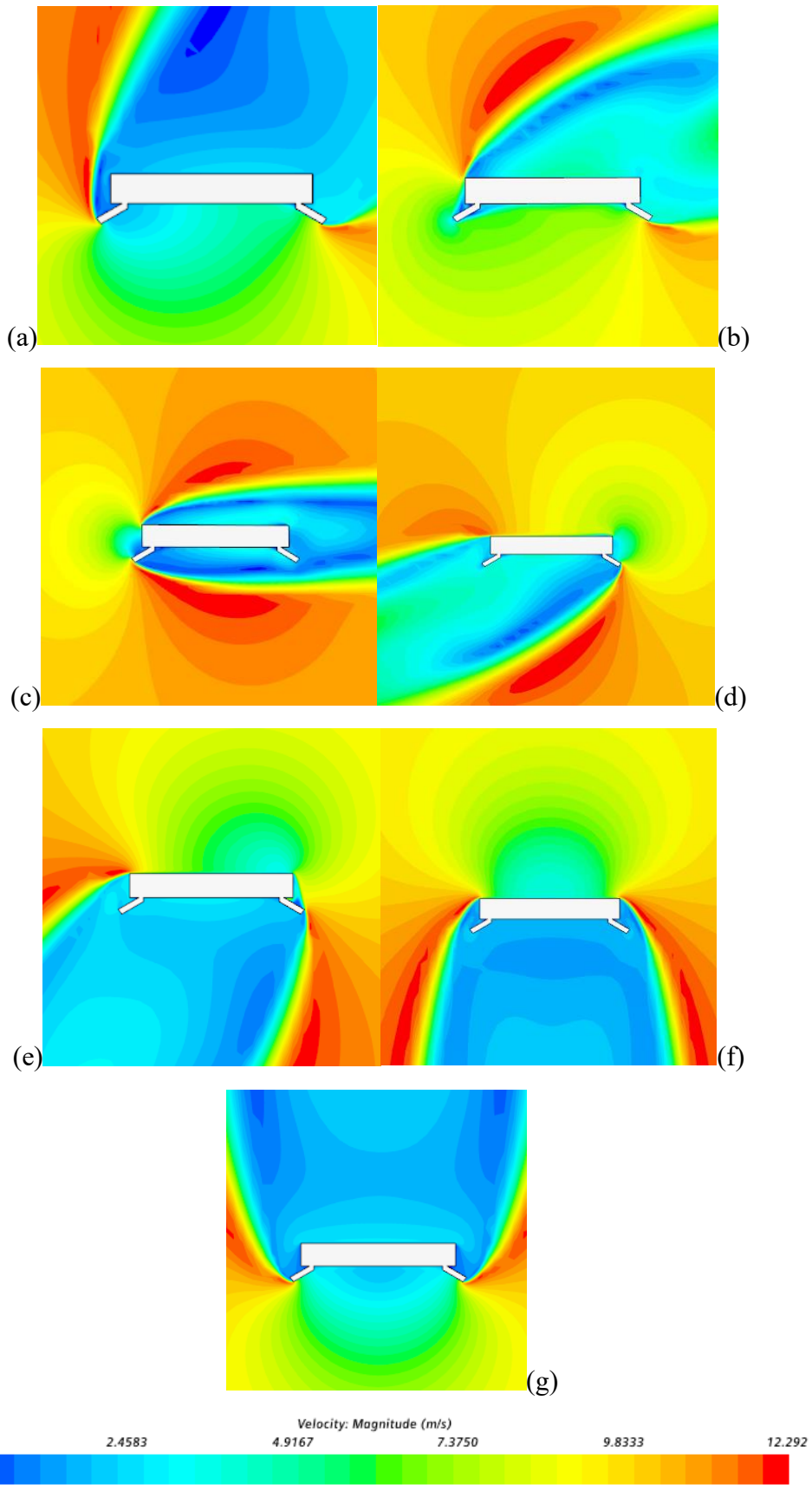


Figure 4.12 Velocity fields: $\frac{\pi}{6}$ for (a), $\frac{\pi}{3}$ for (b), $\frac{\pi}{2}$ for (c), $\frac{2\pi}{3}$ for (d), $\frac{5\pi}{6}$ for (e), π for (f) and 0 for (g).

4.2.2 Evaluation of characteristic length

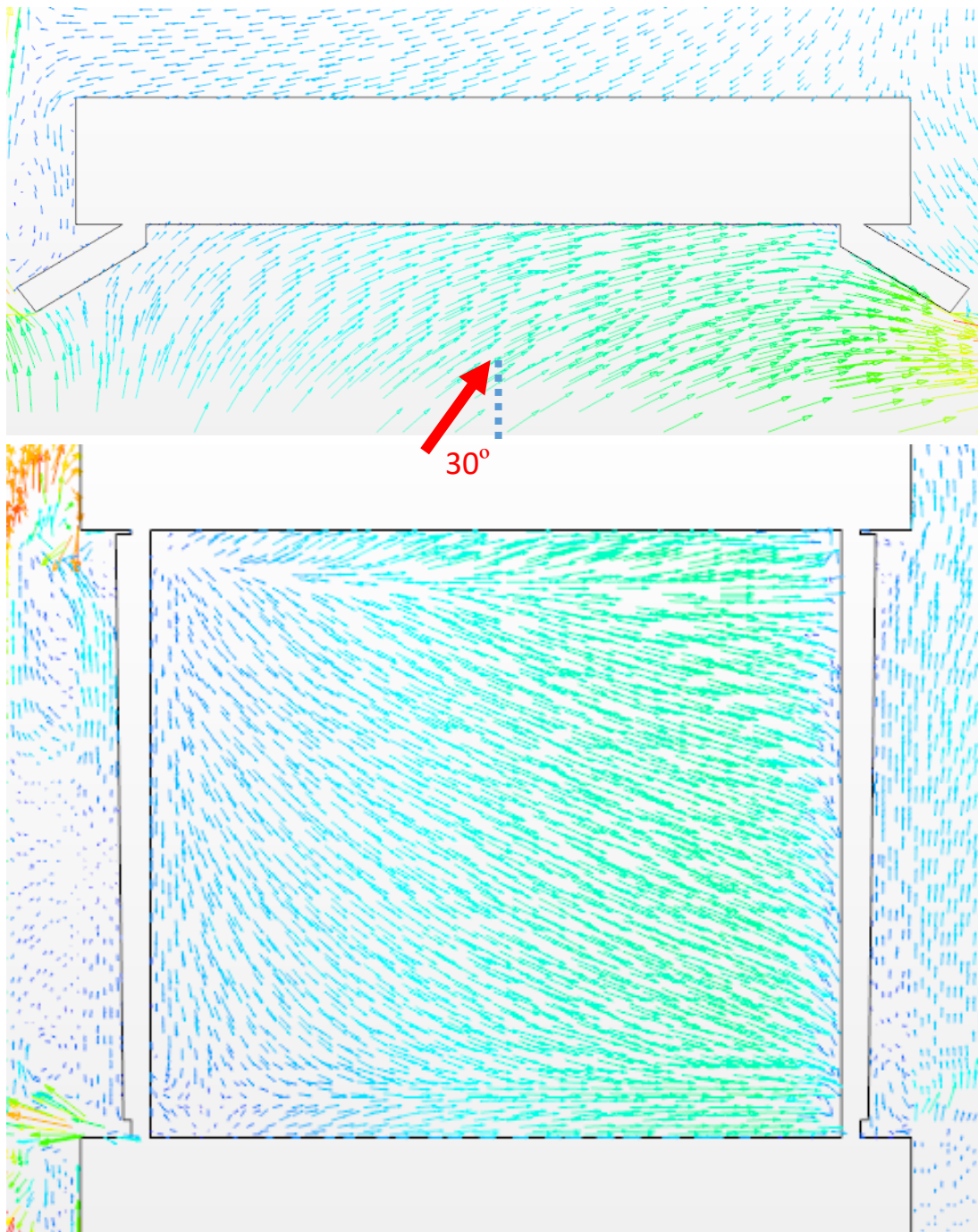


Figure 4.13 Velocity field on horizontal section and parallel plane to the surface at 30°

In Figure 4.13, it shows the computed results for velocity vector fields respectively on equatorial plane and the plane paralleling to the hot surface when the wind direction is emphasized by red arrow with 30° incidence angle with respect to the frontal direction which is indicated by blue dotted line.

Small area of vortexes is observed at the top and bottom area that has been analyzed in the

previous section. But the main air flow goes diagonally through the whole area of the surface so that the characteristic length should be as in Eq. (15):

$$L_c = \sqrt{H^2 + W^2} \quad (15)$$

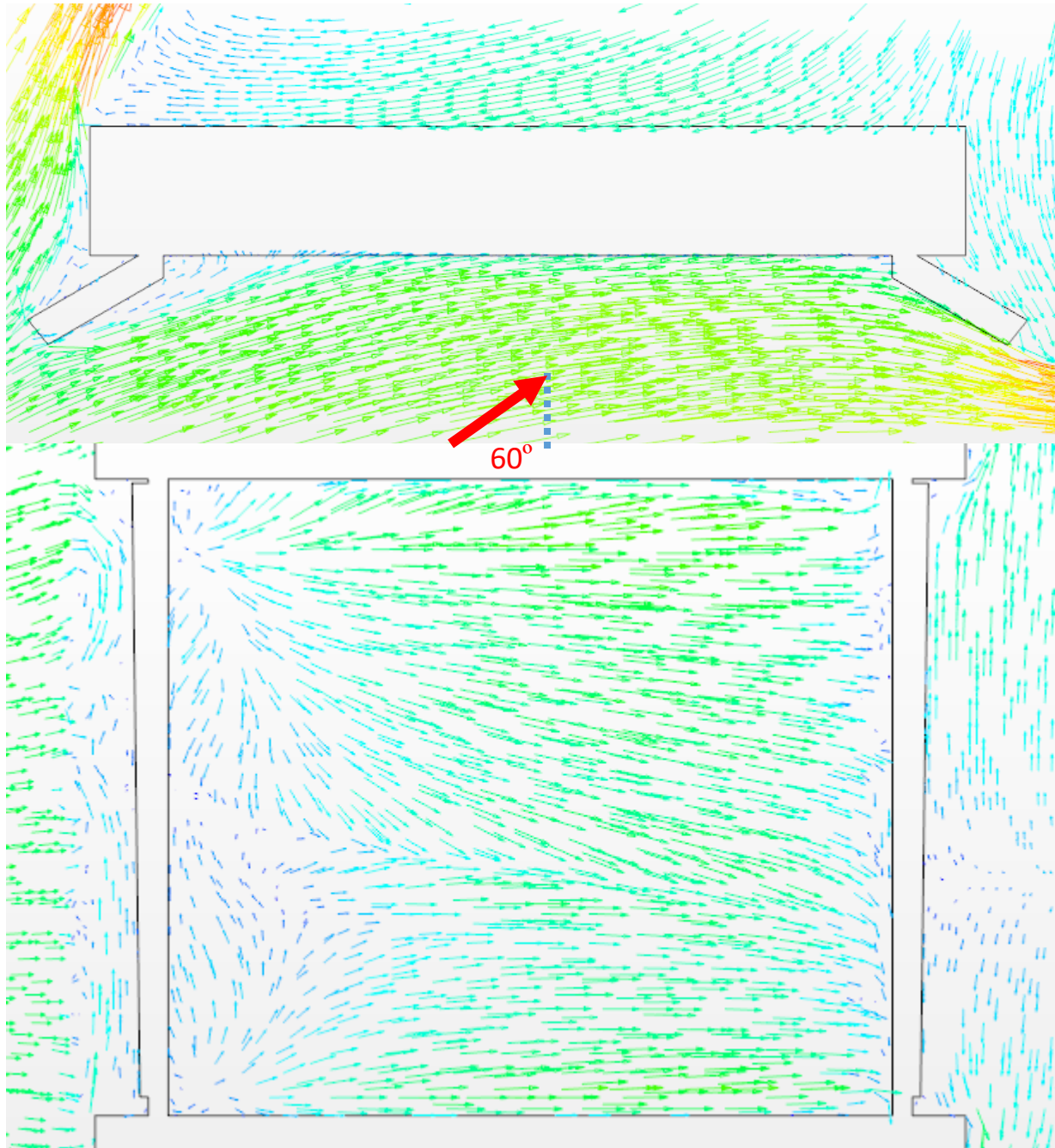


Figure 4.14 Velocity field on horizontal section and parallel plane to the surface at 60°

As showed in Figure 4.14, because of a sink structure between the lateral wing and the hot surface, there is a triangle area of vortex at the left side, but the real hindrance of the lateral

wings is still not being turned on for the wind direction is tangent to the wing.

There seems like a dividing line in the middle of the surface making half of the height as one term for the characteristic length as shown in Eq. (16):

$$L_c = \sqrt{W^2 + \left(\frac{H}{2}\right)^2} \quad (16)$$

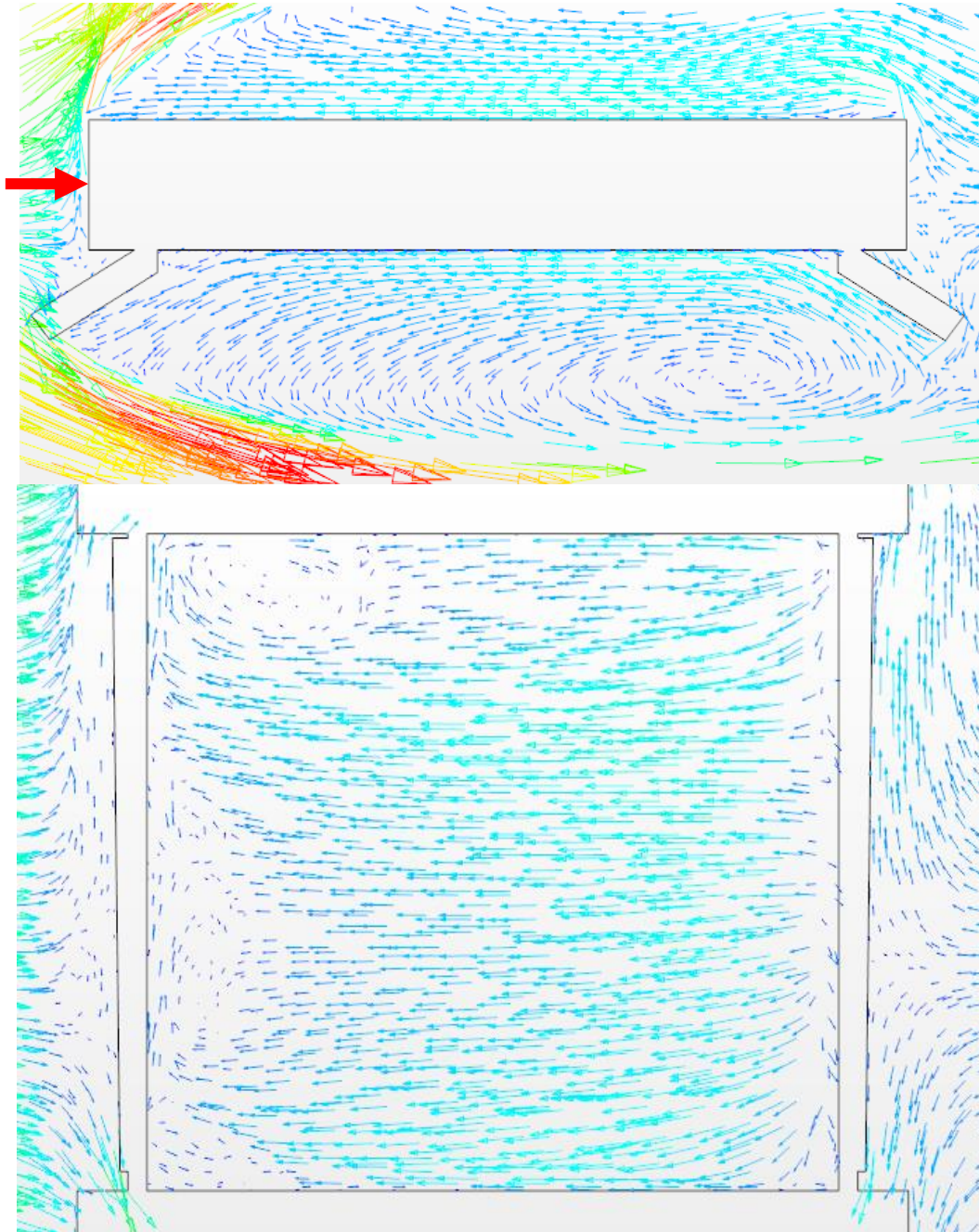


Figure 4.15 Velocity field on horizontal section and parallel plane to the surface at 90°

From Figure 4.15 it shows that as the wind is coming from side way, the lateral wing is shielding away the wind from directly contacting with the hot surface. It is the backflow of a

big vortex with a lower velocity magnitude that flows along the surface horizontally for which the characteristic length should be assumed as in Eq. (17):

$$L_c = \sqrt{W^2} \quad (17)$$

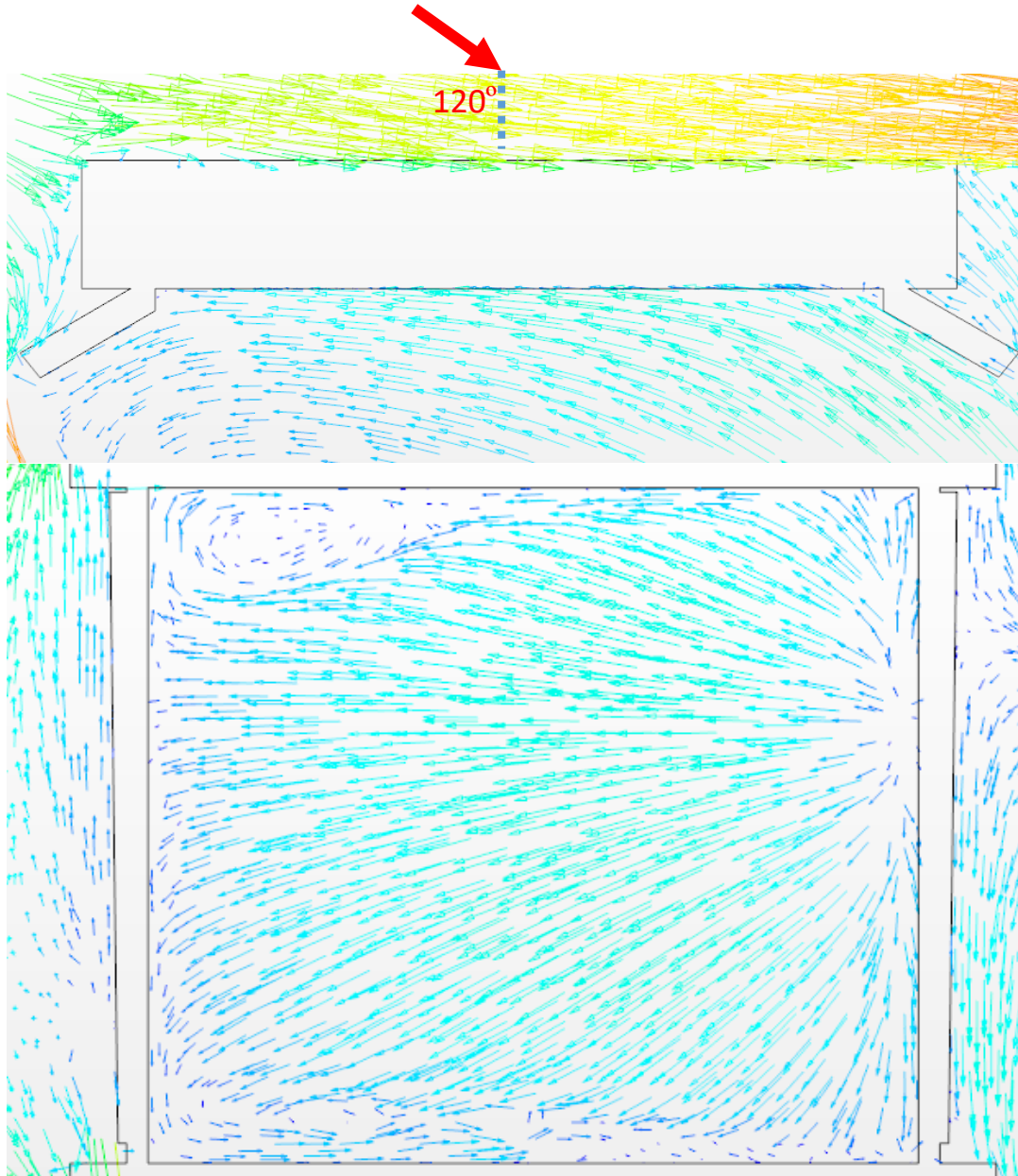


Figure 4.16 Velocity field on horizontal section and parallel plane to the surface at 120°

After observing from Figure 4.16, we can learn that like the condition for 90°, the back flow is making contact with the surface. The movement of the air stream is combining the horizontal direction and the direction along the height of the surface but nearly half up and half down. The characteristic length is presumed to be as in Eq. (18):

$$L_c = \sqrt{W^2 + \left(\frac{H}{2}\right)^2} \quad (18)$$

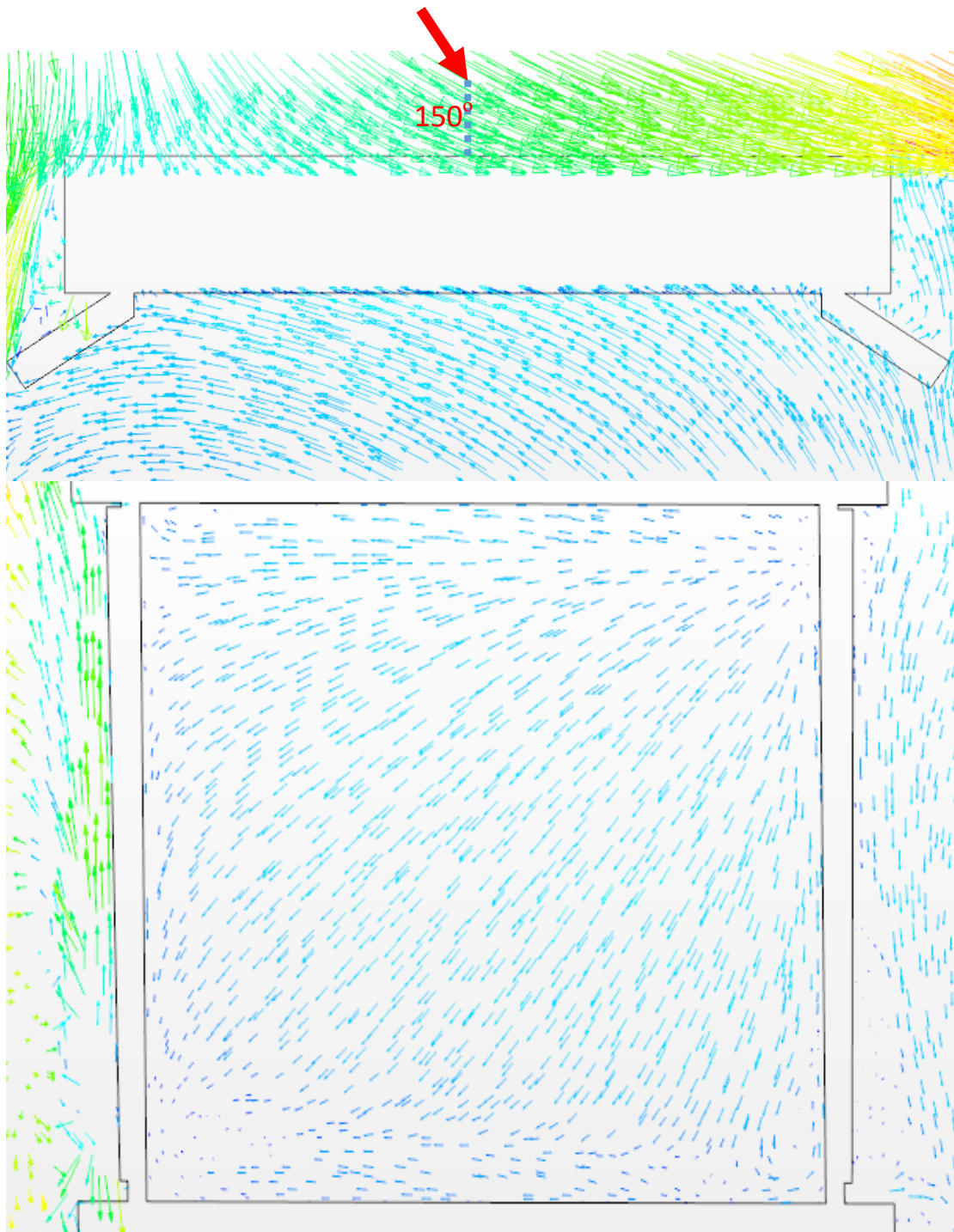


Figure 4.17 Velocity field on horizontal section and parallel plane to the surface at 150°

Comparing Figure 4.17 with Figure 4.12, it seems like a mirror image, so the characteristic length is given in Eq (19):

$$L_c = \sqrt{H^2 + W^2} \quad (19)$$

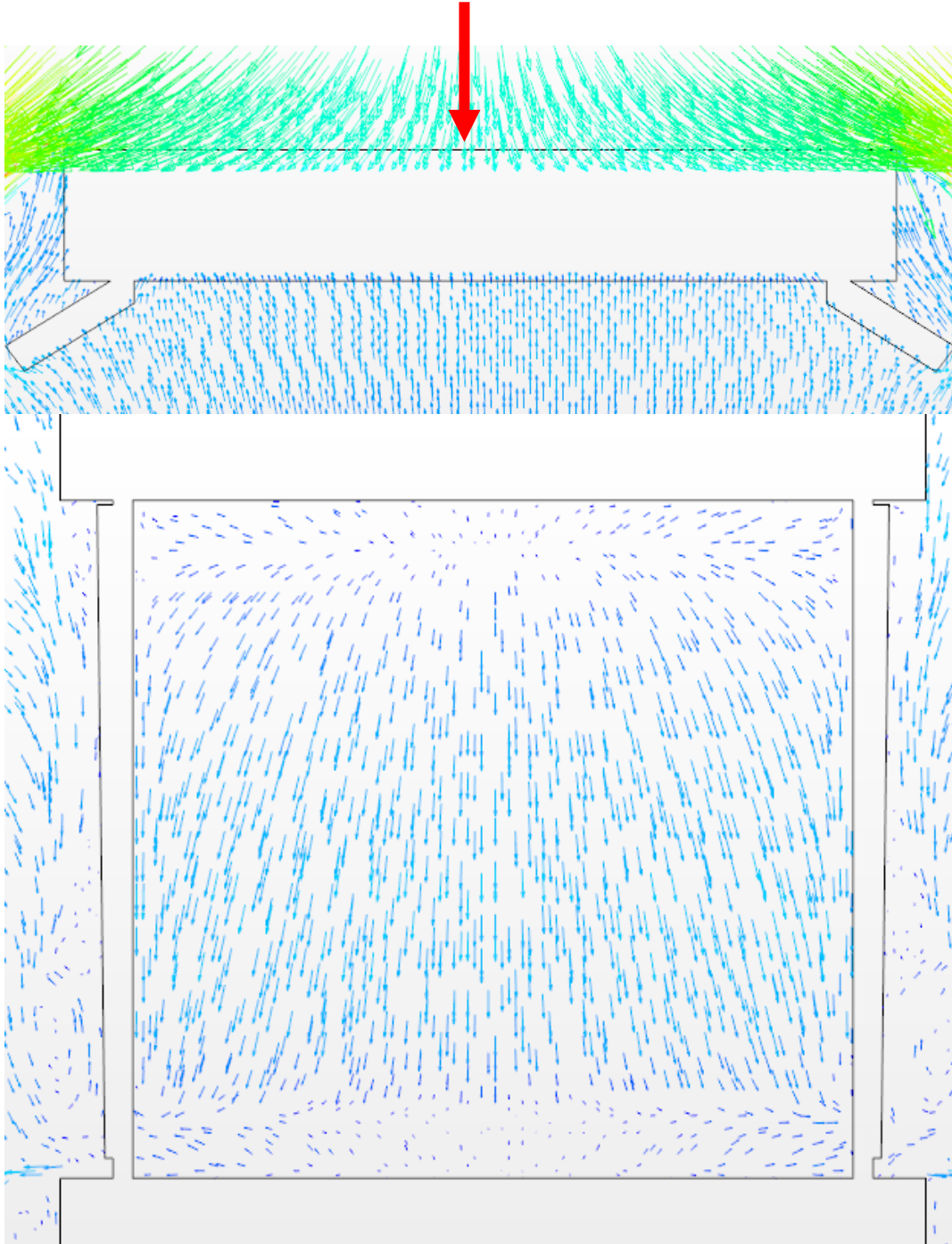


Figure 4.18 Velocity field on horizontal section and parallel plane to the surface at 180°

As showed in Figure 4.18, the velocity field for 180° is similar with the one for frontal direction, the characteristic length is the same as given in Eq. (20):

$$L_c = \sqrt{H^2 + \left(\frac{W}{2}\right)^2} \quad (20)$$

4.2.3 Similarity of characteristic length correlated to incidence angle

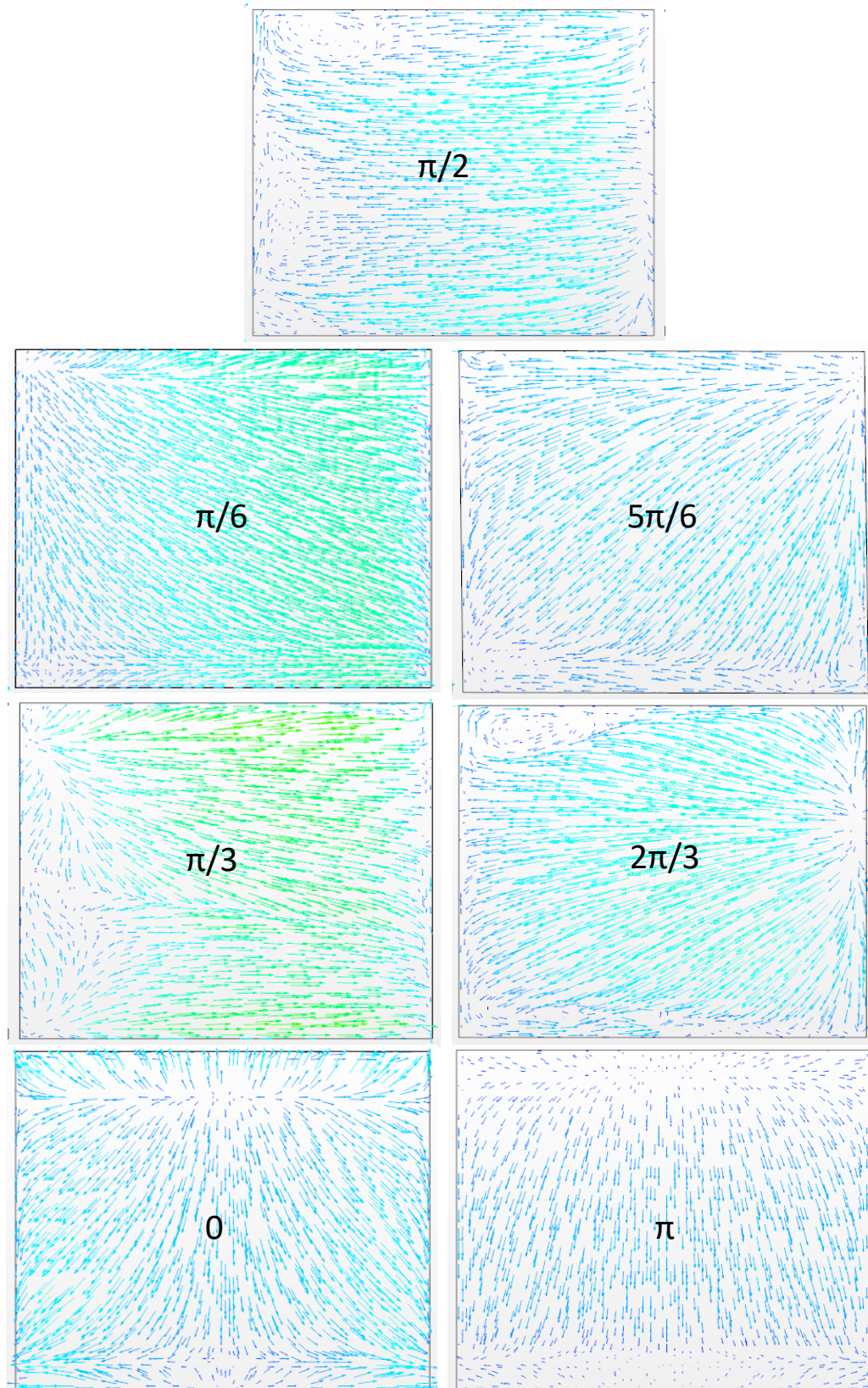


Figure 4.19 Display for velocity fields of parallel section

Surprisingly, there is a similarity between frontal wind and back wind that in Figure 4.19, three pairs of velocity fields are arrayed together to make it better being observed. The sum of each pair's incidence angle equals to π . And for each pair, characteristic length is the same that can be referred to in Table 4.3.

Table 4.3 Directional characteristic length

	0	$\pi/6$	$\pi/3$	$\pi/2$	$2\pi/3$	$5\pi/6$	π
L_c	$\sqrt{H^2 + (\frac{W}{2})^2}$	$\sqrt{H^2 + W^2}$	$\sqrt{W^2 + (\frac{H}{2})^2}$	$\sqrt{W^2}$	$\sqrt{W^2 + (\frac{H}{2})^2}$	$\sqrt{H^2 + W^2}$	$\sqrt{H^2 + (\frac{W}{2})^2}$

4.2.4 From HTC to Nu correlations

The procedure to get Nusselt number is the same as what has been done in chapter three for the frontal wind applying the concluded results for characteristic length from the previous section. Before moving on to find Nu correlations as function of Reynolds number with dependency on incidence angles, some qualitative research on Nu values under the influence of temperature, wind incidence angle as well as its intensity has been conducted as follows.

First, to better analyze the effect from each variable, the condition when temperature is constant at 907K is presented in Figure 4.20 from which both the influence from the angle and the intensity of the wind can be found.

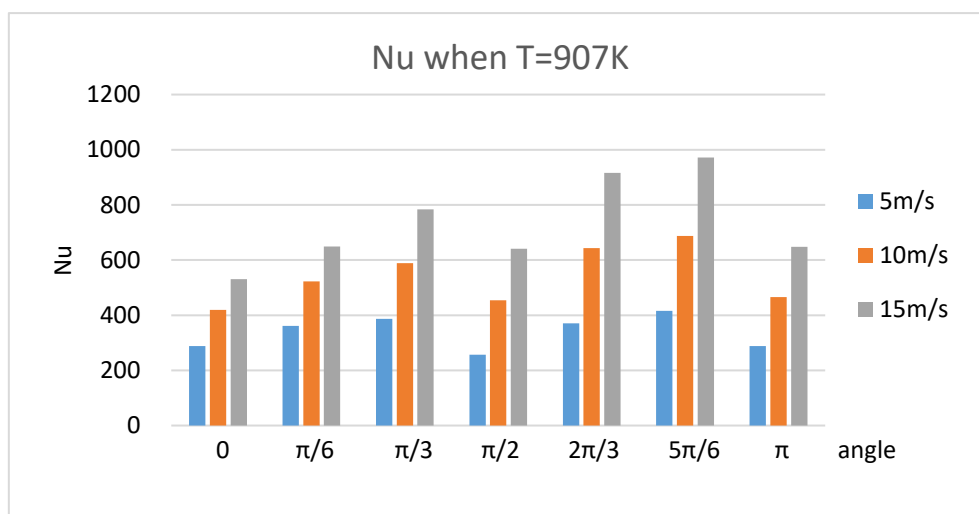


Figure 4.20 Nu trend for directional wind when T=907K

As the angle increases from 0 to $\pi/3$ with respect to the frontal position, the Nusselt numbers are increasing and they reach to the peak at $\pi/3$; then they drop down when the angle comes to $\pi/2$, afterwards they go up again at $2\pi/3$ and even more at $5\pi/6$; to the end, they decrease at π . The above is the Nu trend corresponding to the angle while from the perspective of wind intensity, Nu values increase as the wind becomes stronger.

Then we take the situation when the angle equals to $\pi/6$ as an example to see the trend of Nusselt number as temperature increasing, see Figure 4.21.

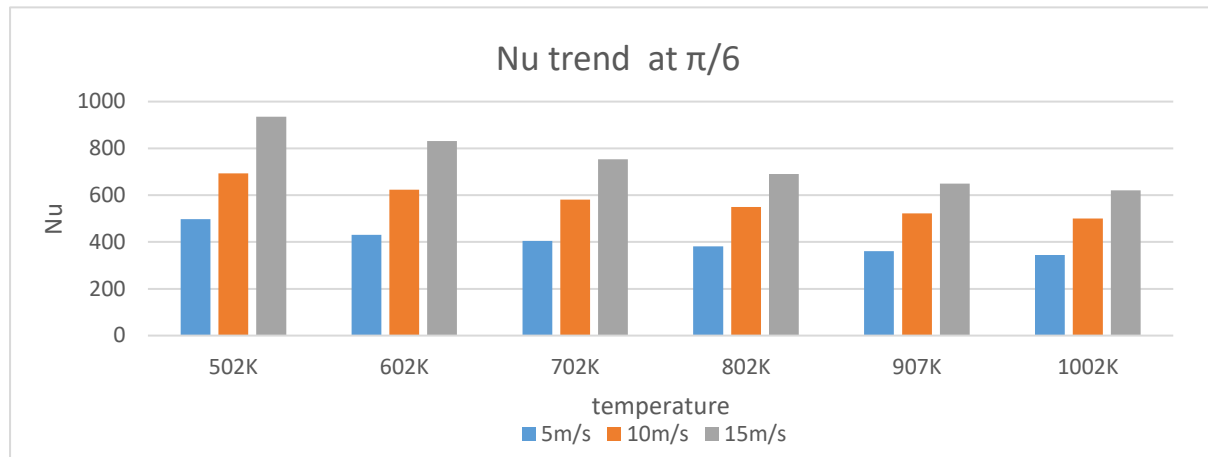


Figure 4.21 Nu trend at different temperature at $\pi/6$

As the temperature of the irradiated surface goes up, the Nusselt number goes down no matter how big the wind intensity is. From observing Figure 4.20, it has been figured that the wind intensity has a positive affect on Nu value which is also confirmed in Figure 4.21. What's more, it can be noticed that the change rate from wind intensity is getting bigger when temperature decreases or it also can be said that high surface temperature would benefit to have a relative lower Nu with limited influence from the wind.

The results when intensity of the wind is 5m/s are presented in Figure 4.22 that provides a relatively comprehensive view based on the whole Nusselt numbers.

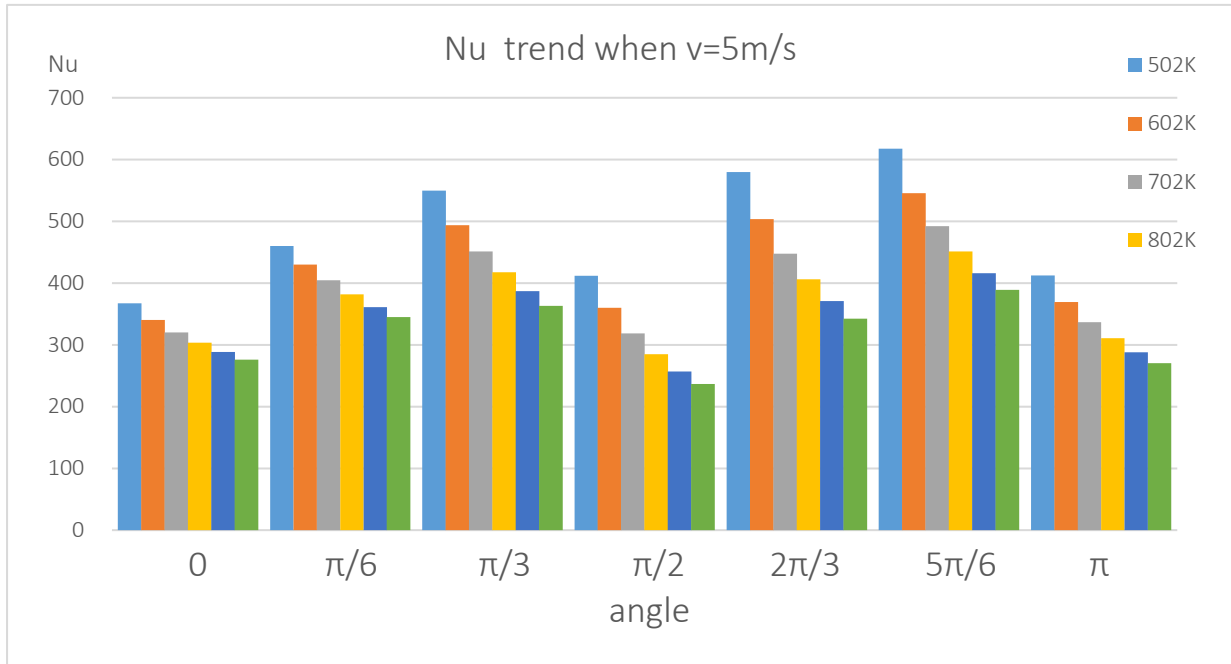


Figure 4.22 Nu trend for directional wind when v=5m/s

After adding the symmetric values for the other half circle, Nu polar plot can be obtained as shown in Figure 4.23. The tendency mentioned before can be better revealed in this plot that it reaches to a valley at 0 , $\pi/2$ and π ; the rest of the positions show bigger Nusselt numbers and the peak is getting at $5\pi/6$.

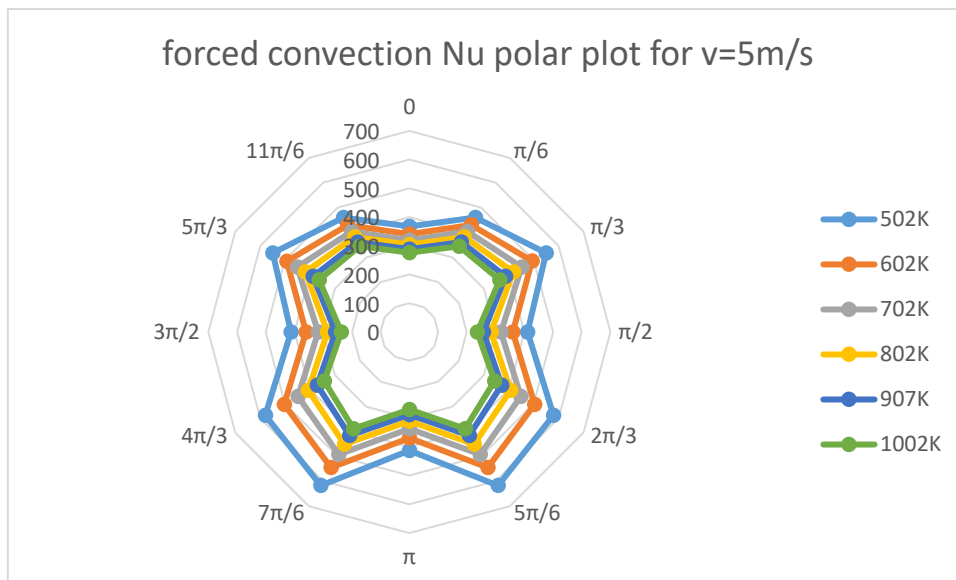


Figure 4.23 Nu polar plot for v=5m/s

Now it is time to do the quantitative analysis solely on the angles. All linear fits respectively for different angles from 0 to π are shown in Figure 4.24.

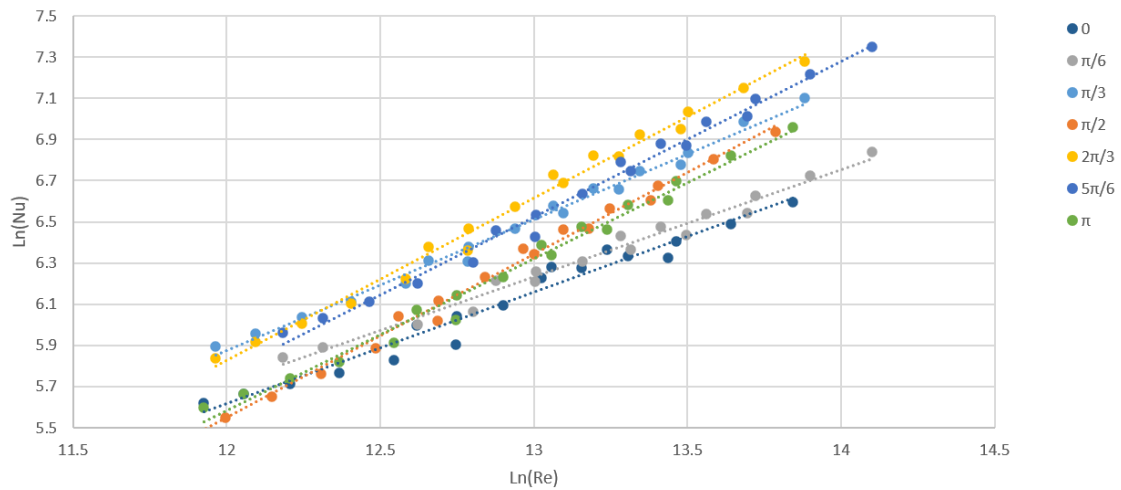


Figure 4.24 Ln (Nu) as function of ln (Re) plot for different incidence angles

It can be noticed that the line for 0 and the line for $\pi/6$ are close to each other; while the rest lines share similar slop.

Tentatively I will divide them into two major groups according to how the lateral wings divide the space that being demo graphed as in Figure 4.25.

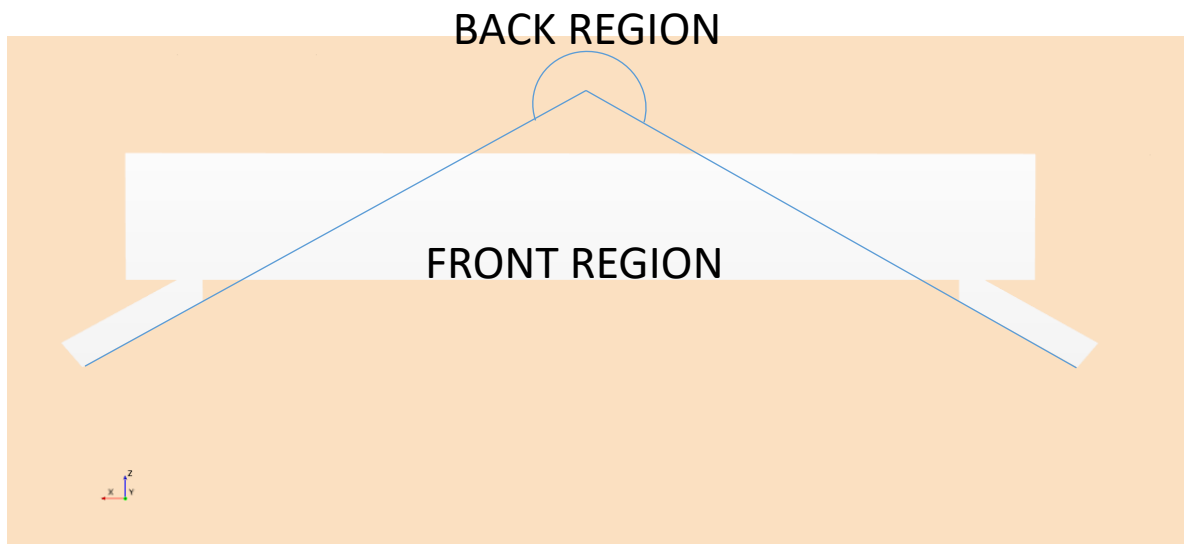


Figure 4.25 Distribution of front region and back region

According to Figure 4.25, all the incidence angles that being analyzed in this work can be divided into two groups: 0, $\pi/6$, $\pi/3$ belongs to front region; $\pi/2$, $2\pi/3$, $5\pi/6$ and π belongs to back region.

Better indication is presented in Figure 4.26 that then seperately fit for front region and back region, the results are showed in Figure 4.27 and Figure 4.28.

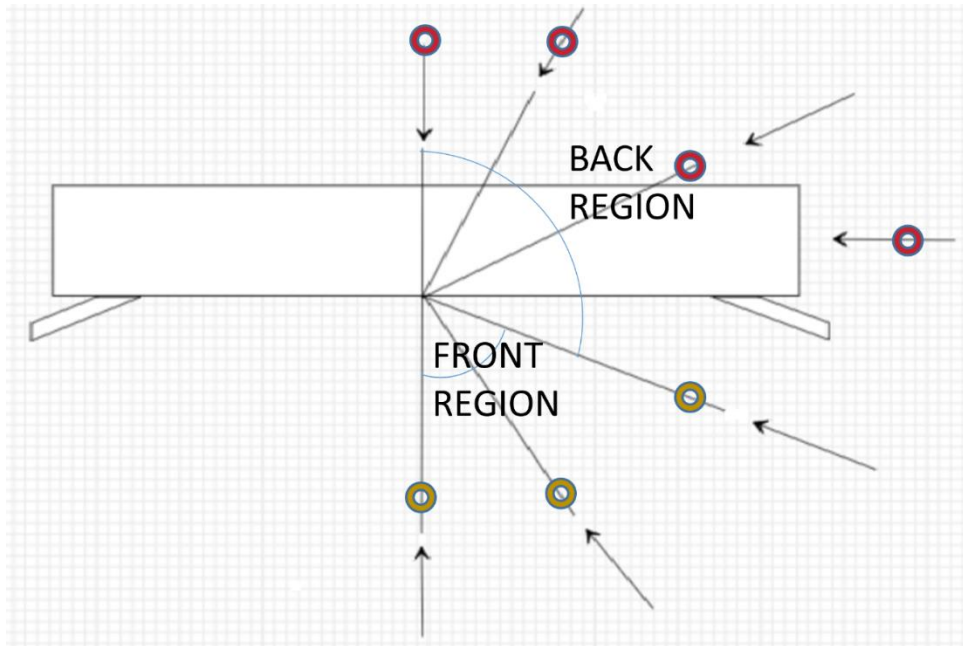


Figure 4.26 Analyzed incidence angles grouping

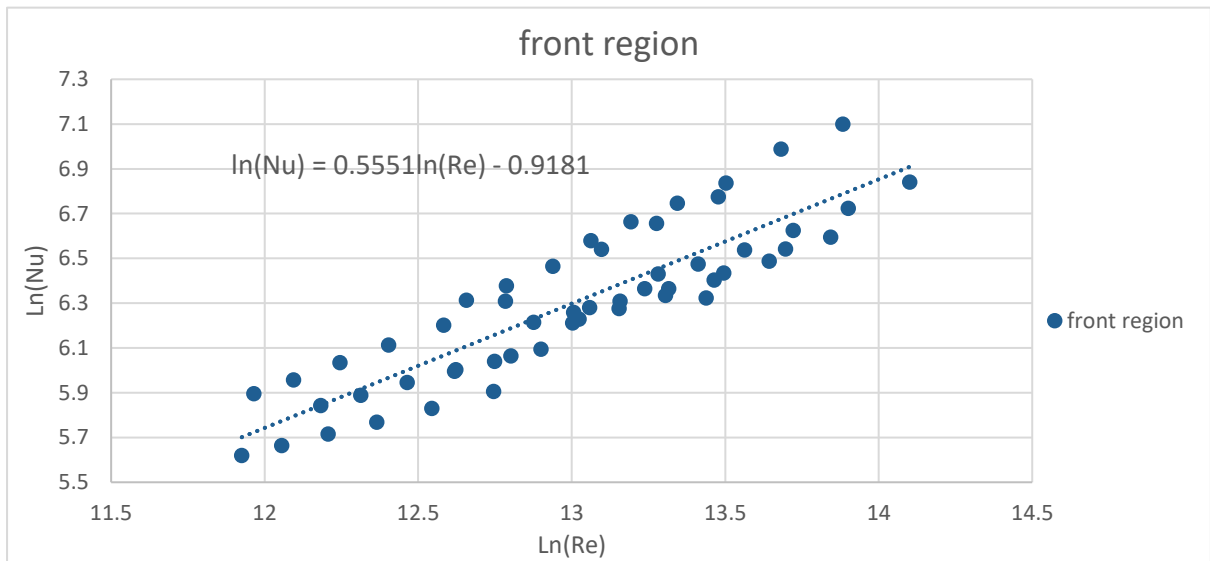


Figure 4.27 Ln (Nu) as function of ln (Re) plot for front region

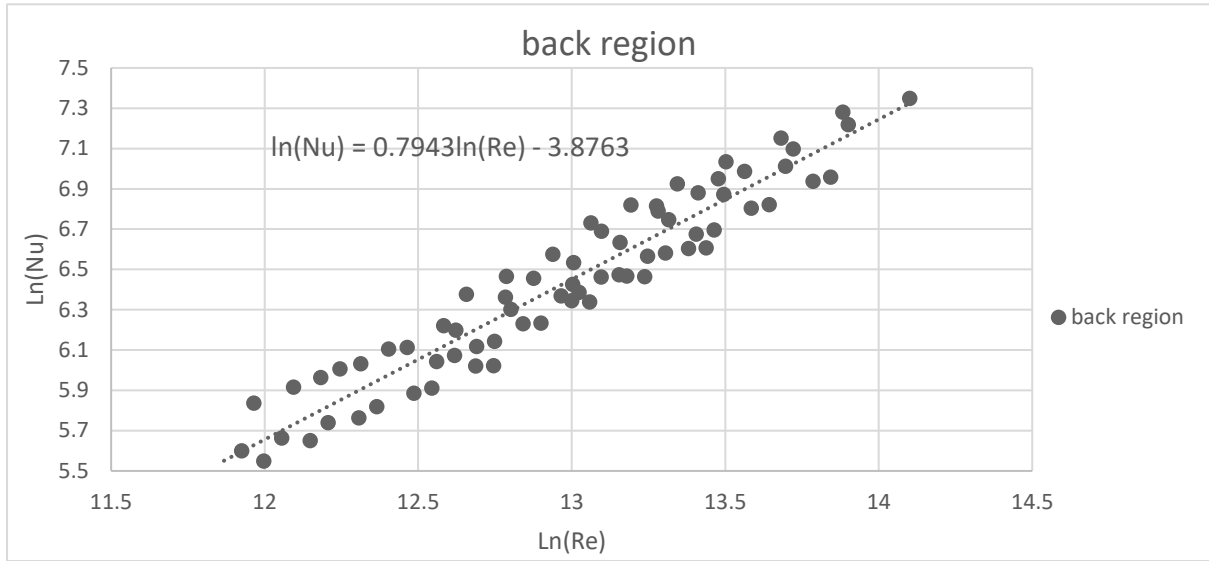


Figure 4.28 Ln (Nu) as function of ln (Re) plot for back region

By using the parameters of the linear fit formulas in Figure 4.27 and Figure 4.28, the Nu correlation can be obtained:

$$Nu_{f_front} = 0.454Re^{0.555}Pr^{1/3} \quad (21)$$

$$Nu_{f_back} = 0.0236Re^{0.794}Pr^{1/3} \quad (22)$$

In Figure 4.27, the slope is a little bit higher than that of the linear line for frontal wind because of the data points from $\pi/6$ and 0 are close to each other even though the ones from $\pi/3$ are in some level distanced.

While in Figure 4.28 the slope of the fit line is higher and basically all the data points are closer.

CHAPTER FIVE

ANALYSIS OF LOSSES IN MIXED FLOW

REGIME

In natural environment, it is the mixed convection happening in most of the situations. In this chapter, the analysis has been focused on mixed convection that is a combination of free convection and forced convection which have been studied in chapter three and chapter four. The main purpose of this chapter is that in the end, it is feasible to check the reliability of the correlations from previous chapters by comparing with the results from simulations.

5.1 Mixed convection estimation

In 1981, a formula was proposed by Incropera and De Witt^[14] as

$$Nu_{mixed} = (Nu_{nat}^{3.2} + Nu_{forc}^{3.2})^{1/3.2} \quad (23)$$

In (23), Nu_{mixed} is Nusselt number for mixed convection that can be expressed as the function of Nusselt number for natural convection Nu_{nat} and for forced convection Nu_{forc} .

In chapter three, the Nu_{nat} has been concluded based on the assumption that the characteristic length equals to the height of the surface while in chapter four the values of Nu_{forc} have been predicted when differed characteristic lengths corresponding to each incidence angle of the wind. But with the difficulty to determine the characteristic length for mixed convection, it is unable to verify the results by using this formula.

Another method to estimate mixed convection according to Siebers^[16] as

$$HTC_{mixed} = (HTC_n^{3.2} + HTC_f^{3.2})^{1/3.2} \quad (24)$$

In (24), HTC_{mixed} is mixed convection heat transfer coefficient that is a combination of natural convection heat transfer coefficient HTC_n and forced convection heat transfer coefficient HTC_f . The exponent value 3.2 is recommended for an external type of receiver.

From previous chapters, the correlation for Nu_{nat} and Nu_{forc} have been acquired and by using Eq. (2), it is able to have the values for HTC_n and HTC_f respectively. After this, a contrast between HTC_{mixed} from the correlation and from the simulation can be made.

At this point, 4 simulations with random choices of angle, wind speed and surface temperature are conducted.

5.2 Simulation setting and the main features of the computed results

The random choices for angle, speed and temperature are presented in Table 5.1 and then the main features from simulations have also been presented afterwards.

Table 5.1 Random simulation parameters setting

	Case 1	Case 2	Case 3	Case 4
Angle	25	45	135	175
Wind speed	3	7	9	12
temperature	527	642	714	939

The velocity fields of these 4 cases are presented in Figure 5.1.

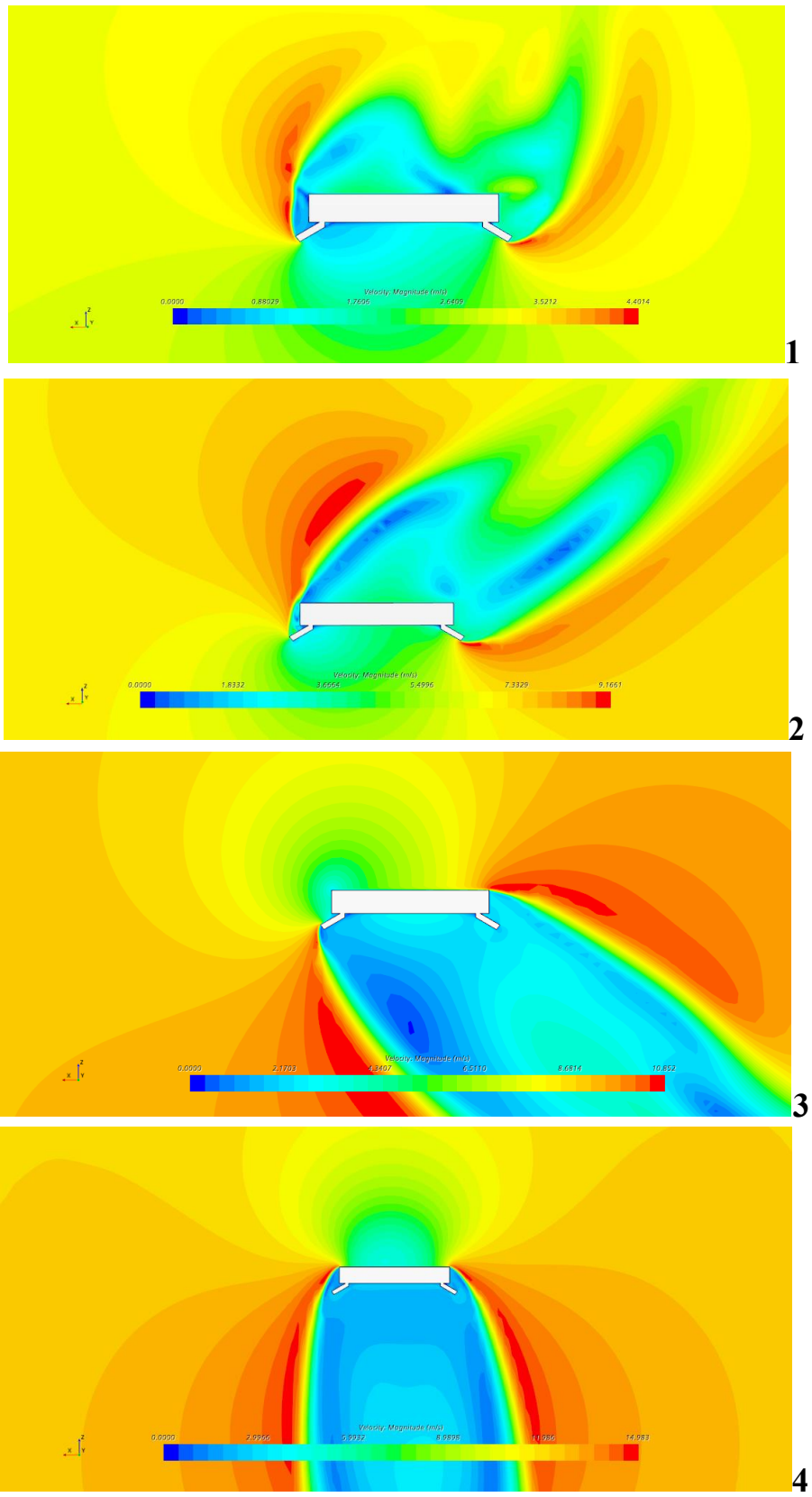


Figure 5.1 Velocity fields:1 for Case 1, 2 for Case 2, 3 for Case 3 and 4 for Case 4

The comparison of HTC from simulations and from the correlations respectively as well

as Nusselt numbers is showed in Table 5.2. The post processing has been done by using the following equations.

The values for HTC from simulations are acquired directly from the report of HTC in the CFD software while that from correlations are calculated according to Eq. (24):

$$HTC_{mixed} = (HTC_n^{3.2} + HTC_f^{3.2})^{1/3.2} \quad (24)$$

In Eq. (24) HTC_n is derived from Eq. (2) with combination of Nu_{nat} that from Table 3.2.

$$Nu = HTC * L/k \quad (2)$$

The reverse of Eq. (2) can be expressed as Eq. (25):

$$HTC_n = Nu_{nat} * k/L \quad (25)$$

The same procedure is applied to get HTC_f by Eq. (26):

$$HTC_f = Nu_{forc} * k/L \quad (26)$$

In Eq. (25) and Eq. (26), Nu_{nat} and Nu_{forc} are obtained from the correlation Eq. (21) and Eq. (22) from the previous chapter respectively, k is valued from film temperature and L is getting from Table 4.3.

The results for HTC_n and HTC_f are then being substitute in Eq. (24) and then HTC_{mixed} form the correlations are obtained. Nu_{mixed} at the end of Table 5.2 are acquired by using Eq. (2) and L is estimated as conventional value as in Eq. (27):

$$L = \sqrt{H * W} \quad (27)$$

Table 5.2 Comparison of HTC and Nu_{mixed}

	Case 1	Case 2	Case 3	Case 4
Angle	25	45	135	175
Wind speed	3	7	9	12
Temperature	527	642	714	939
HTC from simulations	6.01	9.84	13.59	16.16
HTC from correlations	6.66	10.18	13.56	15.74
Error on HTC	10.8%	3.7%	-0.02%	-2.6%
Nu_{mixed} from simulations	282	415	540	548
Nu_{mixed} from correlations	312	429	538	534
Error on Nu_{mixed}	10.6%	3.3%	-0.4%	-2.5%

The errors of HTC between simulations and correlations are listed at the last line of Table 5.2 in which the maximum error is 10%. And the errors for mixed Nusselt number are very similar with those for HTC.

According to what has been presented above, the reliability of the developed correlations for natural convection and forced convection have been confirmed.

CHAPTER SIX

CONCLUSIONS

All the works that have been done here is for developing correlations to estimate the heat losses of the receiver with specific geometry and configuration.

On the basic of previous study on this topic, a CFD model to analyze thermodynamic behavior near the receiver can be set up by which the computational results can be acquired under variable boundary conditions and different uniform temperature for the surface of the receiver. Above all, the simulations for free convection were conducted and by using the output data, a correlation procedure was made and eventually what we have is a Nusselt number correlation on dependency of Rayleigh number.

After the analysis of free convection losses, the simulations were set up for the situation that directional wind with respect to the receiver is presenting and they were running with gravity off so that the buoyancy is killed and the computational results that we get are from pure forced convection.

Before developing correlation procedure for forced convection, the determination of characteristic length is becoming crucial. From the thermodynamics point of view, boundary layers have been observed from temperature fields and velocity vector fields on the plane section that paralleling to the irrational surface with a suitable distance were derived because it is the most direct way to find out how the air move along the surface of the receiver. Surprisingly, a similar behavior of air fluid has been discovered between the cases whose wind incidence angles are supplementary.

As the characteristic lengths have been determined, the Nu correlation procedure can be

carried out. With all the combinations of three differed wind intensities and six different surface temperatures as well as seven directions of the wind, the data acquired was abundant to figure some patterns for how these parameters influencing heat convective losses while as the main focus in this work is the wind effect, Nu dependency of Reynolds number for different wind incidence angles with respect to the receiver were analyzed and then a more simplified classification for incidence angles was made trying to make a more general conclusion and prediction for Nu correlations.

At the end of this work, a mixed convection analysis was made with the hope that the correlations that have been developed before could be confirmed by comparing with the results from simulations. It is satisfying that the maximum error was up to 10%. By completing the comparison, a comprehensive and thorough analysis has been accomplished in all domains.

In perspective, an improvement can be made by taking 75° into account for higher accuracy of Nu correlation because this angle is the critical angle that when performing bigger angle the lateral wing is acting fully as a barrier and the surface is shielded without the direct contact with the wind. Or a totally new study targeting on the influence by removing the lateral wings and overhang can also be conducted.

All in all, it would be great if this work can be a reference for the further investigating on this topic.

ACKNOWLEDGEMENTS

I would like to thank for the careful guidance and help from prof. Laura Savoldi. Her professional opinions have always been my inspiration whenever I run into difficulties during this work. And I benefit and enjoy from the encouragement when it got some big progress.

I also want to thank Marco Lanzani for his help at the beginning of this work.

I am grateful that by using HPC@Polito, time I took for the simulations had been shorten maximally.

Last but not the least, I will give my sincere thanks to my mother that her consistent solicitude is a big driving force for me.

REFERENCES

- [1]. Guardian. Concentrated solar power could generate ‘quarter of world’s energy’.
- [2]. Kraemer Susan. (2017). CSP Doesn't compete with PV-it competes with gas.solarPACES. <https://www.solarpaces.org/csp-competes-with-natural-gas-not-pv/>
- [3]. solarPACES. (2018). How CSP works: Tower, trough, Fresnel or Dish. solarPACES. <https://www.solarpaces.org/how-csp-works/>
- [4]. https://en.wikipedia.org/wiki/Solar_power_tower
- [5]. Behar, O., Khellaf, A., Mohammedi, K., 2013. A review of studies on central receiver solar thermal power plants. *Renew. Sustain. Energy Rev.* 23, 12–39.
- [6]. Michel J. Bignon. (1980). The Influence of the Heat Transfer Fluid on the Receiver Design. *Electric Power Systems Research*, 3 (1980) 99 – 109
- [7]. Ávila-Marín, A.L., 2011. Volumetric receivers in solar thermal power plants with central receiver system technology: a review. *Sol. Energy* 85, 891–910. <https://doi.org/10.1016/j.solener.2011.02.002>.
- [8]. Logie, W.R., Pye, J.D., Coventry, J., 2018. Thermoelastic stress in concentrating solar receiver tubes: a retrospect on stress analysis methodology, and comparison of salt and sodium. *Sol. Energy* 160, 368–379. <https://doi.org/10.1016/j.solener.2017.12.003>.
- [9]. Boerema, N., Morrison, G., Taylor, R., Rosengarten, G., 2013. High temperature solar thermal central-receiver billboard design. *Sol. Energy* 97, 356–368. <https://doi.org/10.1016/j.solener.2013.09.008>.
- [10]. ["Jemalong CSP Pilot Plant – 1.1MWe"](#). Vast Solar. Retrieved 24 April 2021.
- [11]. Marco Lanzani. 2019. Modelling of the heat losses from a sodium-cooled receiver for small scale CSP applications.
- [12]. M. Cagnoli, A. de la Calle, J. Pye, L. Savoldi, R. Zanino, 2019. Sol. A CFDsupported dynamic system-level model of a sodium-cooled billboard-type receiver for central tower CSP applications. *Energy* 177, 576-594.
- [13]. Australian Government – Bureau of Meteorology, 2018. Meteo Data [WWW Document]. http://www.bom.gov.au/climate/averages/tables/cw_065016.shtml.
- [14]. Incropera and De Witt, et al. 2006. Fundamentals of heat and mass transfer. John Wiley & Sons. 6th edition.
- [15]. Siebers, D.L., J. S. Kraabel, 1984. Estimating convective energy losses from solar central receivers. Sandia report
- [16]. Siebers, D.L., Moffatt, R.F., Schwind, R.G., 1982. Experimental mixed convection from a large, vertical plate in a horizontal flow. In 7th International Heat Transfer Conference. Munich, West Germany